



Potential Antidiabetic Compounds from *Anogeissus leiocarpus*: Molecular Docking, Molecular Dynamic Simulation, and ADMET Studies

Mubarak Muhammad Dahiru ^{1*} 

Neksumi Musa ² 

AbdulAzeez Mumsiri Abaka ² 

Maimuna Abdulrahman

Abubakar ³ 

¹ Department of Pharmaceutical Technology, Adamawa State Polytechnic, Yola, Adamawa, Nigeria

² Department of Science Laboratory Technology, Adamawa State Polytechnic, Yola, Adamawa, Nigeria

³ Department of Biochemistry, Modibbo Adama University, Yola, Adamawa, Nigeria

*email: mubaraq93@gmail.com

Keywords:

Anogeissus leiocarpus
ADMET
Diabetes
Molecular docking
Molecular dynamics

Abstract

This study aimed to evaluate the antidiabetic potential of compounds from *Anogeissus leiocarpus* *in silico* and the potential of the compounds as antidiabetic drug candidates. Molecular docking (MD), molecular dynamics simulation (MDS), and ADMET were carried out *in silico* to evaluate the compounds' antidiabetic potential and drug candidacy. The MDS revealed the least BA (-8.7 kcal/mol) was exhibited by Compound X (palmitic acid) with Glucagon-like Peptide-1 Receptor (GLP1), while the highest BA (-5.8 kcal/mol) was demonstrated by I (1,2,4-benzetriol) with dipeptidyl peptidase IV (DPP-4) among the best interactions. The MDS result showed good docked complexes' flexibility, deformability, and stability with low eigenvalues ranging from 8.52×10^{-5} to 1.30×10^{-4} . All the compounds had a bioavailability score of 0.55 except VI (0.85), while the synthetic ability showed a good score of ≤ 3.01 . Eight compounds were predicted to be soluble, with two poorly soluble. Additionally, all the compounds had high gastrointestinal absorption, with the majority being blood-brain barrier permeant, while skin permeation value was between -2.55 and -7.48 cm/s. Furthermore, none of the compounds were either permeability glycoprotein (P-gp) substrate or CYP2C19 and CYP2C9 inhibitors, though some were CYP1A2, CYP2D6, and CYP3A4 inhibitors. Moreover, the toxicity study showed moderate to non-toxicity results with toxicity classes between 3 and 5. Conclusively, the compounds from *A. leiocarpus* showed good binding interactions, which are the protein targets of antidiabetic therapy and potentially good candidates for antidiabetic drug development.

Received: May 16th, 2023

1st Revised: August 25th, 2023

Accepted: August 27th, 2023

Published: August 30th, 2023



© 2023 Mubarak Muhammad Dahiru, Neksumi Musa, AbdulAzeez Mumsiri Abaka, Maimuna Abdulrahman Abubakar. Published by Institute for Research and Community Services Universitas Muhammadiyah Palangkaraya. This is an Open Access article under the CC-BY-SA License (<http://creativecommons.org/licenses/by-sa/4.0/>). DOI: <https://doi.org/10.33084/bjop.v6i3.5027>

INTRODUCTION

Diabetes is a multifactorial physiological disorder with macrovascular and microvascular complications resulting in cardiovascular diseases, retinopathy, neuropathy, nephropathy, blindness, and kidney failure, which might lead to fatality¹. It is characterized by persistent hyperglycemia resulting from a disturbance in insulin secretion, function, or both, extremely upsetting the body's normal metabolic activities and affecting the body's energy sources with notable symptoms including polyuria, polydipsia, and hunger¹. There are two main types of diabetes: type 1 and type 2 diabetes. The former is regarded as insulin-deficient, while the latter is insulin-resistant². Worldwide, diabetes continues to be devastating and a leading menace in decreasing the quality of life, resulting in mortality, morbidity, and a burden on individuals, healthcare, and government spending³. Diabetes affects 537 million people, including three in every four adults in middle- and low-income countries, with mortality due to diabetes estimated to be up to 6.7 million people in 2021. The number of people living with diabetes is predicted to be 643 million by 2030, with further projections indicating a rise to 783 million by 2045^{3,4}.

How to cite: Dahiru MM, Musa N, Abaka AM, Abubakar MA. Potential Antidiabetic Compounds from *Anogeissus leiocarpus*: Molecular Docking, Molecular Dynamic Simulation, and ADMET Studies. *Borneo J Pharm.* 2023;6(3):249-77. doi:10.33084/bjop.v6i3.5027

Furthermore, 541 million adults were reported to exhibit impaired glucose tolerance, placing them at high risk of type 2 diabetes². Additionally, in 2021, global diabetic expenditure was estimated to be 966 billion USD, up to a 316% rise in the past 15 years, a figure predicted to rise to 1054 billion USD by 2045⁴.

Globally, therapeutic approaches are employed in managing diabetes, including insulin therapy and biguanide drugs. However, exercise, change in life, and diets are recommended for managing and preventing onset⁵⁻⁷. Additionally, the use of medicinal plants has often been reported, especially in low-income countries with poor access to modern healthcare systems and therapeutics, with poverty contributing to the choice. Although synthetic drugs are prescribed for diabetic patients, factors such as affordability and associated side effects of these drugs make them undesirable for some individuals. However, some approaches, such as multidrug target therapy (combined), are often used in synthetic drug therapy⁸. Side effects such as hypoglycemia, bloating, and diarrhea make synthetic drugs undesirable, pushing patients to seek alternatives to achieve glycemic control and therapeutic goals⁹. Medicinal plants offer an alternative approach to diabetic management considering their synergistic action, often safe, and affordability with minimal side effects¹⁰. The phytochemical contents of these plants play vital roles in targeting different proteins involved in the pathophysiology of diabetes, providing multitargeting of the diseases considering its nature as a multiple disorder¹¹⁻¹³. These proteins also target synthetic antidiabetic drugs for different antidiabetic effects. Several medicinal plants were reported to exhibit antidiabetic effects with their pharmacological properties attributed to their phytochemical compositions^{10,11,14,15}.

Anogeissus leiocarpus tree belongs to the Combretaceae family, growing up to 15-18 m in height, and is native to the savannah in Africa and other parts of the world¹⁶. Different parts of the plant are used to manage diseases in traditional medicine, including tuberculosis¹⁷, trypanosomiasis¹⁸, malaria¹⁹, and wound healing²⁰. Several studies revealed the pharmacological activities of this plant, including *in vivo* and *in vitro* studies including antitrypanosomal²¹, antidiarrheal activity²², antibacterial effects²³, antiangiogenic and antitumor properties²⁴. The nature of diabetes makes it a multitarget disease for different therapeutics to achieve glycemic control and reduce its complications. *Anogeissus leiocarpus* was reported to be rich in phenols and possess strong antihyperlipidemic and antioxidant properties attributed to antidiabetic activities²⁵. Recent *in vitro* and *in vivo* studies^{26,27} reported the antidiabetic properties of *A. leiocarpus*, suggesting different mechanisms without evidence of the molecular interactions of the proteins involved in the pathophysiology of diabetes. Thus, in our study, the antidiabetic potential of *A. leiocarpus* compounds was evaluated *in silico* via molecular docking, molecular dynamics, and ADMET studies to document the molecular interactions of the compounds with proteins involved in the pathology of diabetes and evaluate the potential of the compounds as antidiabetic drugs candidates.

MATERIALS AND METHODS

Materials

The HP laptop (HP Envy M6 K010dx) was used for the present study with hardware specifications including 8 GB RAM with an AMD 2.1 GHz to 2.9 GHz Elite Quad-core A10-5745M accelerated processor and AMD Radeon HD 8610G graphics with up to 3053 MB total graphics memory. The ligands used for this study were selected based on their abundance from our previous study²⁸ and retrieved from the PubChem database (<https://pubchem.ncbi.nlm.nih.gov>), while proteins were downloaded from the RSCB protein databank database (<https://www.rcsb.org>). The ligands were downloaded in SDF format and converted to PDB format using the OpenBabel version 3.1.1 software²⁹. In contrast, proteins were downloaded in PDB format, followed by the removal of identical chains, attached ligands, heteroatoms, and water molecules using AutoDock Tools version 1.5.7³⁰. The list of ligands is presented in **Table I**, including their respective PubChem ID and designation, whereas the list of proteins is presented in **Table II** with their RSCB PDB ID.

Table I. List of ligands.

Name	PubChem ID	Designation
1,2,4-benzotriol	10787	Compound I
1,2-epoxyhexadecane	23741	Compound II
2-(tetradecyloxy) ethanol	16491	Compound III
2-methoxyhydroquinone	69988	Compound IV
5-hydroxymethylfurfural	237332	Compound V
5-methyl-1H-pyrazole-3-carboxylic acid	9822	Compound VI
Hexadecanal	984	Compound VII

Maltol	8369	Compound VIII
Methyl 14-methylpentadecanoate	21205	Compound IX
Methyl palmitate	8181	Compound X

Table II. List of target enzymes.

Name	RSCB PDB ID
Protein tyrosine phosphatase 1B (PTP1B)	2ZMM
11- β -hydroxysteroid dehydrogenase (HSD1)	3D3E
Peroxisome proliferator-activated receptor γ (PPAR γ)	4EMA
α -amylase (AA)	3BAJ
Dipeptidyl peptidase IV (DPP-4)	3W2T
Glucagon-like peptide 1 receptor (GLP1)	7S15
Sodium-glucose cotransporter-2 (SGLT2)	7VSI
α -glucosidase (AG)	3WEN

Methods

Molecular docking

The MD of ligands with proteins was performed using the Vina wizard of PyRx virtual screening Tool version 0.8 software. The ligands and proteins were converted to PDBQT format before the docking with exhaustiveness set to 32. The dock poses of each ligand-protein interaction were saved in PDB format for 3D visualization using PyMOL software version 2.5.4, with the lowest binding affinity interactions saved for further analysis³¹. The 2D interactions of the best dock poses were visualized by LigPlot+ 2.2.8 for hydrogen bonds (HBs) and hydrophobic interactions (HBIs), while the while protein-ligand interaction profiler webserver³² was utilized for viewing other interactions. The inhibition constant (K_i) was evaluated from the binding affinity by the formula $K_i = \exp \Delta G/RT$, where the temperature $T=298.15$ K and R depict the universal gas constant 1.985×10^{-3} kcal $^{-1}$ mol $^{-1}$ k $^{-1}$, and ΔG represents the binding affinity³³.

Molecular dynamics simulations

The CABS-flex V2.0 online server (<http://biocomp.chem.uw.edu.pl/CABSflex2/index>)³⁴ and the iMODs server (<https://imods.iqfr.csic.es>) (iMODS)³⁵ were utilized to carry out the MDS. The best protein-ligand docked complexes with the lowest energy were uploaded to the servers in PDB format. The protein interactions' root-mean-square fluctuations (RMSFs) were assessed using the CABS-flex server to evaluate their structural stability via the trajectory or NMR ensemble with the simulation time set to 10 ns while other parameters were set as default. The iMODs were used to determine the stability and molecular motion of the docked protein-ligand complexes to evaluate their structural dynamics and molecular motion. The values of deformability, B-factor, eigenvalues, variance, covariance map, and elastic network were used to evaluate the structural dynamics and stability of the docked complexes.

Absorption, distribution, metabolism, excretion, and toxicity prediction

The present study used a SwissADME online server³⁶ to determine the selected compounds' medicinal chemistry, drug-likeness, lipophilicity, and water solubility in the ADME prediction. The toxicity of the compounds was predicted using ProTox-II online server³⁷ to determine the oral toxicity values, carcinogenicity, hepatotoxicity predicted, cytotoxicity, mutagenicity, and immunotoxicity. Furthermore, the potential of the compounds to cause adverse reactions via binding to proteins was predicted using the ProTox-II.

RESULTS AND DISCUSSION

The binding interactions of PTP1B with the compounds are presented in **Table III** displaying the binding affinity (BA), inhibition constant (K_i), and binding interactions. Compound II (1,2-epoxyhexadecane) exhibited the least BA (-5.9 kcal/mol) and K_i (47 μ M) among the compounds followed by Compound IX (methyl-14-methylpentadecanoate) with a slightly higher BA (-5.8 kcal/mol) and K_i (55 μ M), though both compounds have same HBs (2) and HBIs (10). Compounds VIII and VI demonstrated the highest number of HBs (4) but with slightly inferior BAs (-5.7 and 5.6 kcal/mol respectively) compared to Compounds II and IX. Additionally, Compound X had the highest BA (-4.9 kcal/mol) and K_i (254 μ M).

Table III. Protein tyrosine phosphatase 1B (PTP1B).

Compounds	BA (kcal/mol)	K _i (μM)	HB	HBI
II	-5.9	47	2	10
IX	-5.8	55	2	10
I	-5.7	66	4	4
VII	-5.7	66	1	11
VIII	-5.7	66	4	6
VI	-5.6	78	4	4
III	-5.4	109	3	10
IV	-5.3	129	2	7
V	-5.2	153	3	6
X	-4.9	254	1	6

Note: BA = Binding Affinity, K_i = Inhibition Constant, HB = Hydrogen Bonds, HBI = Hydrophobic Interactions

Figure 1 shows the 2D and 3D interactions of PTP1B with Compounds II and IX, displaying the HB distance in Å, HBIs, and the participating residues with Compound IX demonstrating a slightly longer HB distance. The HBs distances for Compound II were 2.96 Å (Arg47) and 2.81 Å (Asp48), while those of Compound IX were 2.98 and 2.99 Å (Arg221). Both compounds also participated in HBIs interactions with similar residues. The RMSF plots of Compounds II and IX are shown in **Figure 2**. Compound II demonstrated its highest RMSF of 4.305 Å at residue no. 298 (the last residue), the least (0.089 Å) RMSF was seen at residue no. 84 while the maximum RMSF (4.159 Å) observed for Compound IX was at residue no. 183 with the minimum RMSF (0.101 Å) observed at residue no. 213. Furthermore, slightly different fluctuations were observed at residue no. 129, 139, 151, 165, 182, 217, 218, 240, 285, and 298 in both compounds.

Figure 3 presents the iMODs MD simulation results of the docked PTP1B complex. The deformability and B-factor plot of the protein represent the mobility of the residues of PTP1B during the simulation, with each peak pointing to deformability within the protein regions. Higher peaks represent regions of high mobility in the docked complex, while the B-factor plot compares the normal mode analysis (NMA) and PDB field of the complex, whereas the eigenvalues and variance inversely relate to each normal mode 32. The co-relationship between residues within the complexes is represented by the covariance plot correlation motion represented by the red color. In contrast, white represents uncorrelated motions, and blue shows anticorrelation with better stability represented by more significant correlations among residues. The elastic network represents the associations between the atoms with stiffer portions depicted by the darker-gray portions.

Molecular docking considers the interactions of docked complexes, highlighting the types of binding interactions involved to achieve an energy-favorable dock pose. In our study, different enzymes involved in the pathophysiology of diabetes were docked with the compounds previously identified in *A. leiocarpus*. PTP1B is a crucial protein in the insulin signaling pathway that opposes the phosphorylation of the tyrosine subunits of the β units of the insulin receptor and insulin receptor substrate-1 (IRS-1), downregulating the insulin signal in the cell³⁸. Additionally, it is involved in the leptin signaling pathway influencing appetite by dephosphorylating Janus kinase 2 (JAK2), the downstream signaling molecule of leptin. Insulin promotes glucose intake and utilization by cells, while leptin decreases appetite via the JAK2 signaling and promotes energy expenditure³⁹. PTP1B opposes the actions of both insulin and leptin via dephosphorylation, downregulating their activity, thus a target of antidiabetic agents⁴⁰. In our study, Compounds II and IX interacted with PTP1B with the least BA and K_i (**Table III**), participating in 10 HBIs with binding pockets. This might be attributed to the hydrophobic nature of the binding pocket, as both compounds were predicted to be lipophilic. A thiophene-based PTP1B inhibitor was previously reported to inhibit PTP1B with K_i of 4 μM with notable interacting residues such as Arg221, Phe182, and Gln266 forming HBs⁴¹. Compounds II and IX interacted with similar residues, including the formation of HB with Arg221 by IX in addition to the HBIs. The binding of these compounds to PTP1B might disrupt its activity via allosteric inactivation.

Additionally, the MD simulation using CABS-flex showed fluctuations of residues of the docked complex from their original position observed for both compounds, possibly influencing the enzyme's activity. Furthermore, the flexibility of the docked evaluated by the iMODs server showed deformability of the docked complex with considerable mobility as the deformability index was close to 1.0. Thus, further establishing the compounds' binding effect on the enzyme's structure. Flexibility is a considered factor in the interactions of macromolecules with ligands. The eigenvalue signifies the energy required to deform the docked complex, reflecting the motion stiffness of the complex directly proportional to the deformability of the complex⁴². The low eigenvalues observed for PTP1B further signify the stability and flexibility of the complexes.

The binding interactions of HSD1 with the compound showing the BA, K_i , and binding interactions are displayed in **Table IV**. Compound X (methyl palmitate) exhibited the highest BA (-8 kcal/mol) and K_i (1 μ M) next to Compound VIII (maltol) with BA and K_i of -6 kcal/mol and 40 μ M respectively, though Compound VIII had a higher number of HBs (7) but fewer HBIs (4) than Compound IX. Only Compound I participated in PS interaction among all the compounds, while Compounds IV, V, and VII had the highest BA, though with different numbers of HBs and HBIs. Compound V had the same number of HBs as Compound VIII, though with higher BA, while Compounds IX and X had the same numbers of HBIs. The 2D and 3D interactions of HSD1 with Compounds X and VIII are displayed in **Figure 4**, showing the HBs (including the distances in angstrom) and HBIs with the participating residues. Although no HBs were observed for Compound X, the HBs distances of Compound VIII were between 2.86-3.18 Å with participating residues including Asp132, His135, Asn127, Ser125, Met179, and Ala181.

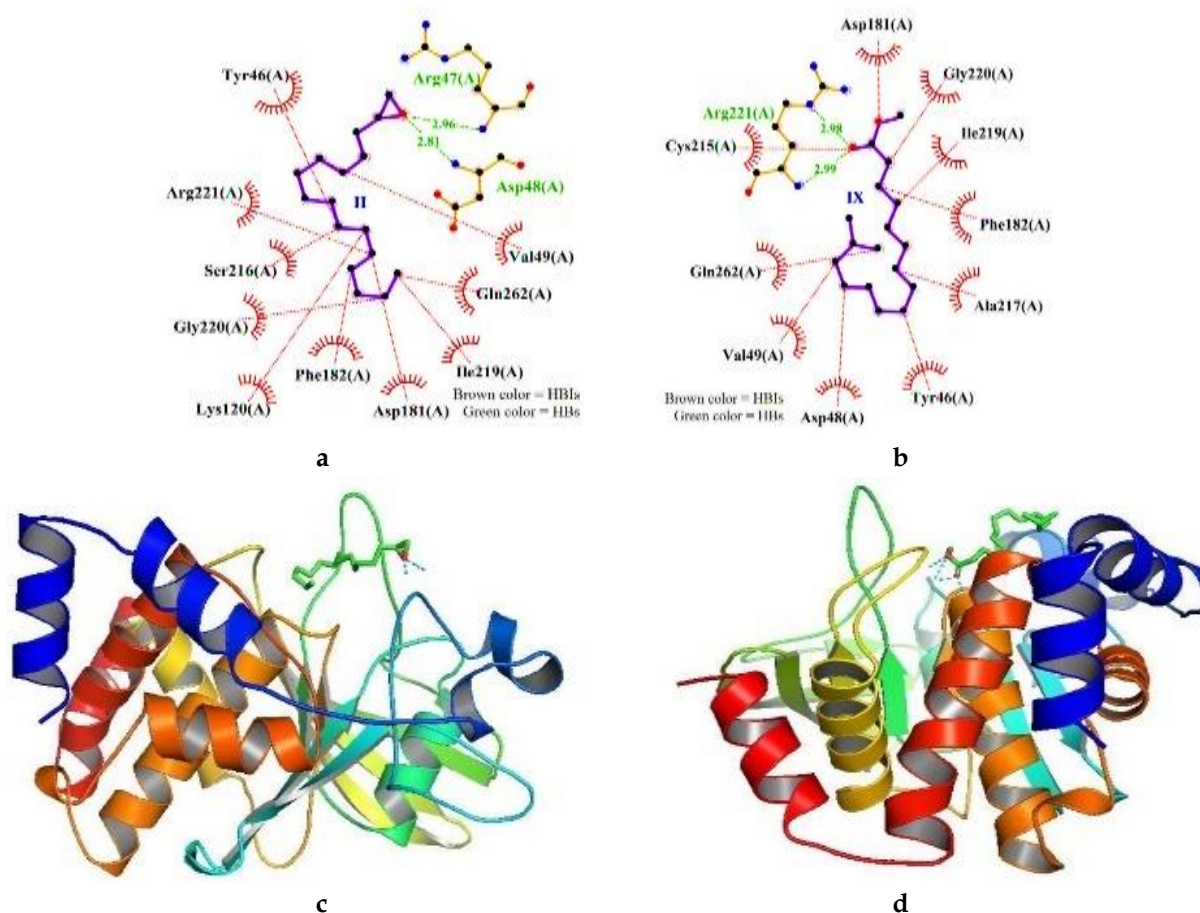


Figure 1. 2D and 3D interactions of PTP1B with Compound II and IX. (a) 2D Compound II; (b) 2D Compound IX; (c) 3D Compound II; and (d) Compound IX.

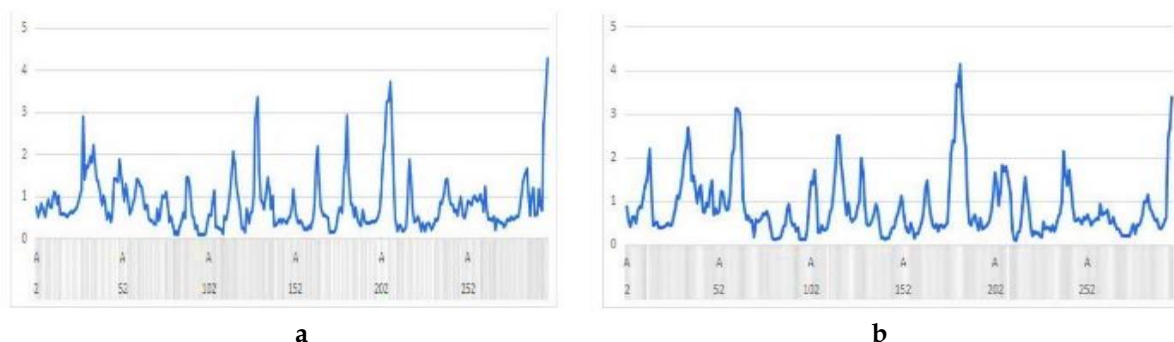


Figure 2. RMSF profile of PTP1B with (a) Compound II; and (b) IX.

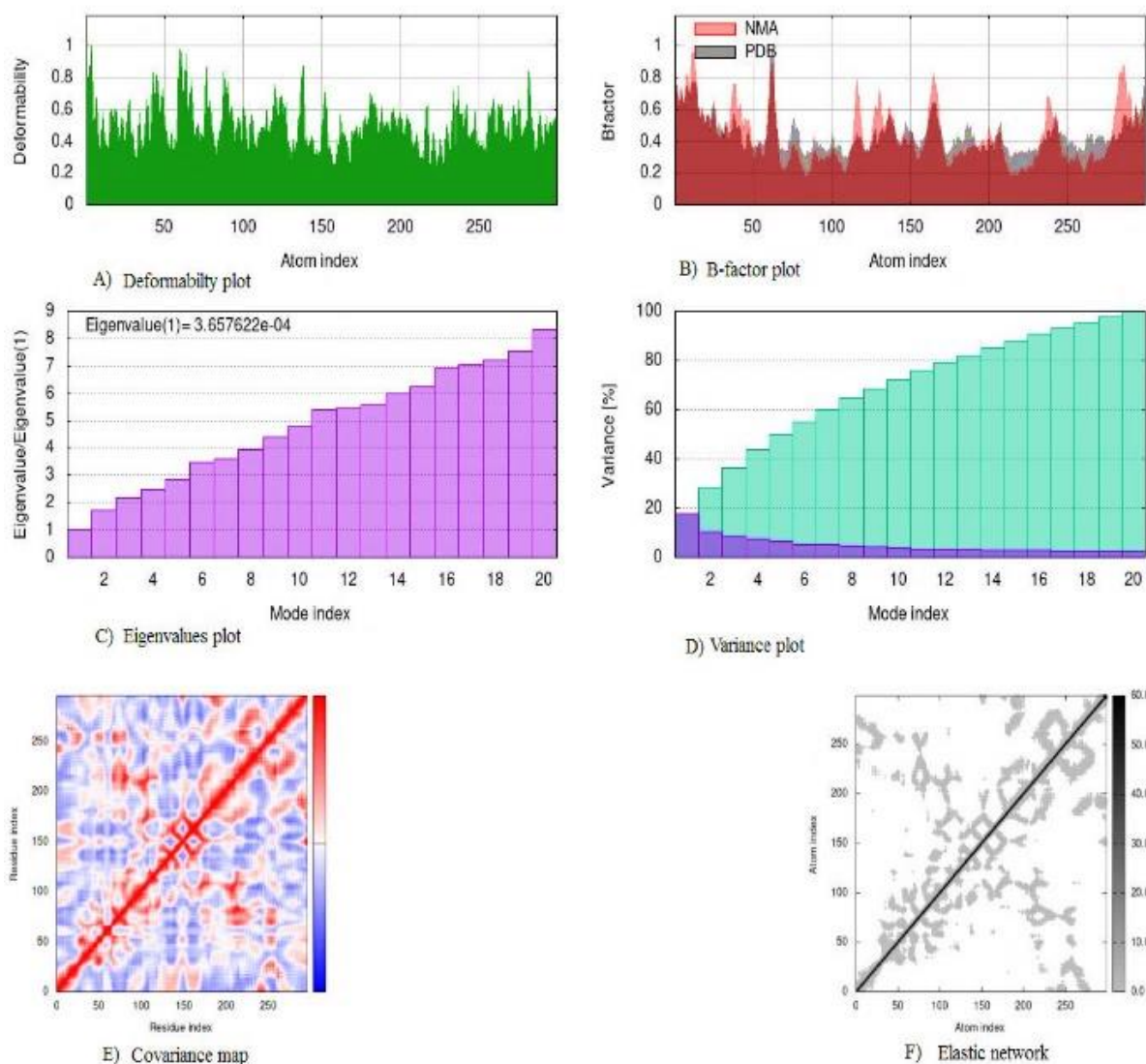


Figure 3. iMODs MD simulation results of PTP1B docked complex.

The RMSF plots of HSD1 with Compounds X and VIII are presented in **Figure 5**. The highest (6.963 Å) fluctuation was observed for Compound X at residue no. 284, the least (0.109 Å) fluctuation was observed at no. 50 and 116. Compound VIII's maximum (7.154 Å) fluctuation occurred at residue no. 21, while the minimum (0.153 Å) was observed at no. 187. However, residue no. 43, 84, 111, 128, 179, 206, 263, and 284 were among the fluctuating residues for Compounds X and VIII. **Figure 6** displays the iMODs MD simulation of the HSD1 docked complex, depicting the deformability, B-factor, eigenvalues, variance, covariance map, and elastic network plots.

Accumulation of glucocorticoids in tissues has been implicated in the development of insulin resistance and type 2 diabetes. Specifically, tissue cortisol level is influenced by HSD1 activity via the conversion of inactive cortisone to active cortisol, thus leading to its accumulation⁴³. Therefore, HSD1 has been targeted by antidiabetic agents to decrease cortisol accumulation by suppressing its activity. In our study, Compound X was observed to bind HSD1 with a low BA and K_i compared to all the other compounds without any HBs interaction. Additionally, it had the highest HBIs observed at the pocket surrounded by helices, coils, and sheets interacting with up to 12 residues. Some benzamide was previously reported to inhibit HSD1 via binding in this pocket⁴⁴ interacting with similar residues (Thr222, Ala223, Tyr183, Ser170, and Gly216) like Compound X though with HBs (Tyr183 and Ser170) interactions absent for Compound X. This is not surprising considering the lipophilic nature of Compound X. Additionally, MD simulations of the Compound X docked complex with CABS-flex show high residues fluctuations which might reflect modification of the enzyme structure, thus its activity.

Similarly, simulation with the iMODs server points to the deformability of the docked complex with a low eigenvalue and deformability index close to 1. Thus, further supporting the structural deformation of the enzyme. Although Compound X had lower BA and K_i than Compound VIII, a superior number of HBs were observed for Compound VIII, indicating a stronger interaction with the enzyme⁴⁵. Thus, Compound VIII might also be a good candidate for HSD1 inhibition, considering its ADME profile, though it has the lowest LD₅₀ among all the compounds.

Table IV. 11- β -hydroxysteroid dehydrogenase (HSD1).

Compounds	BA (kcal/mol)	K_i (μ M)	HB	HBI	PS
X	-8	1	-	12	-
VIII	-6	40	7	4	-
I	-5.7	66	4	8	His135
VI	-5.5	92	2	7	-
III	-5.4	109	5	9	-
IX	-5.4	109	1	12	-
II	-5.1	181	1	11	-
IV	-4.9	254	5	5	-
V	-4.9	254	7	5	-
VII	-4.9	254	1	10	-

BA = Binding affinity, K_i = Inhibition constant, HB = Hydrogen bonds, HBI = Hydrophobic interactions, PS= π -stacking

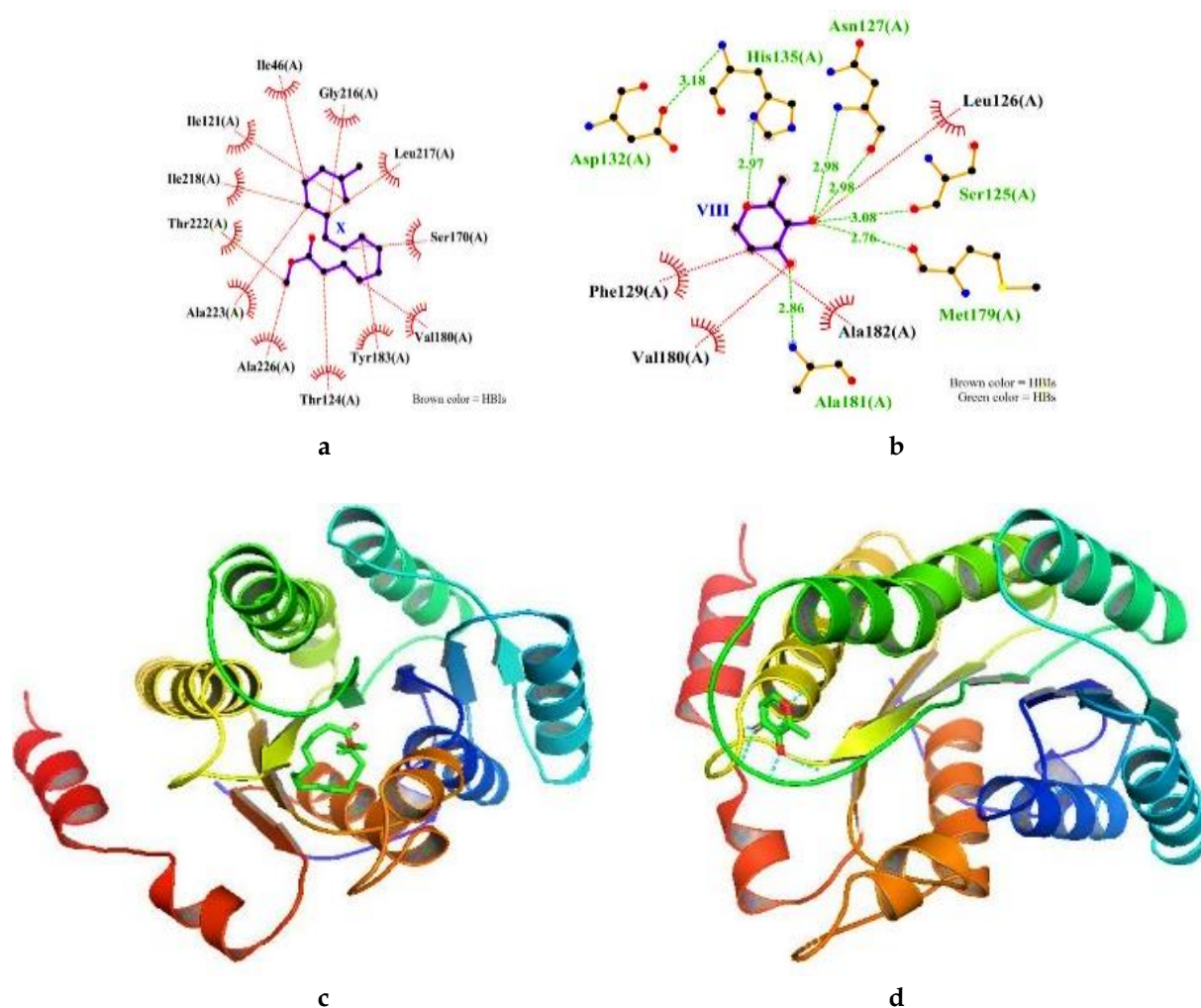


Figure 4. 2D and 3D interactions of HSD1 with Compound X and VIII. (a) 2D Compound X; (b) 2D Compound VIII; (c) 3D Compound X; and (d) Compound VIII.

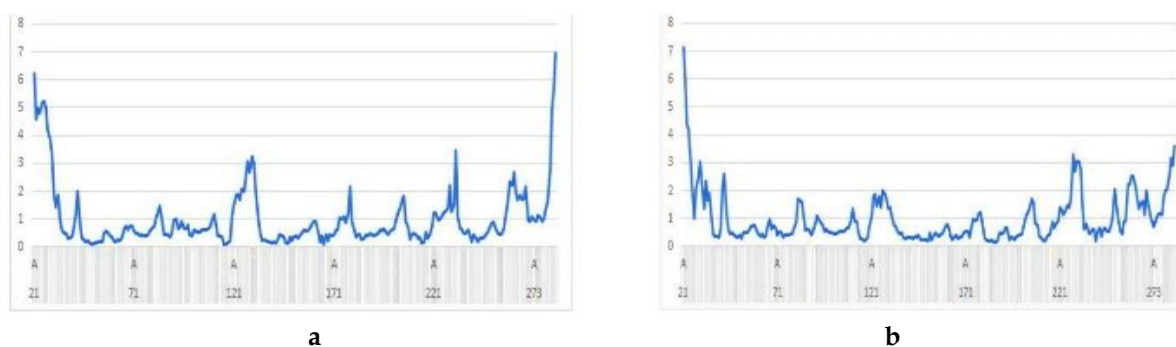


Figure 5. RMSF profile of HSD1 with (a) Compound X; and (b) VIII.

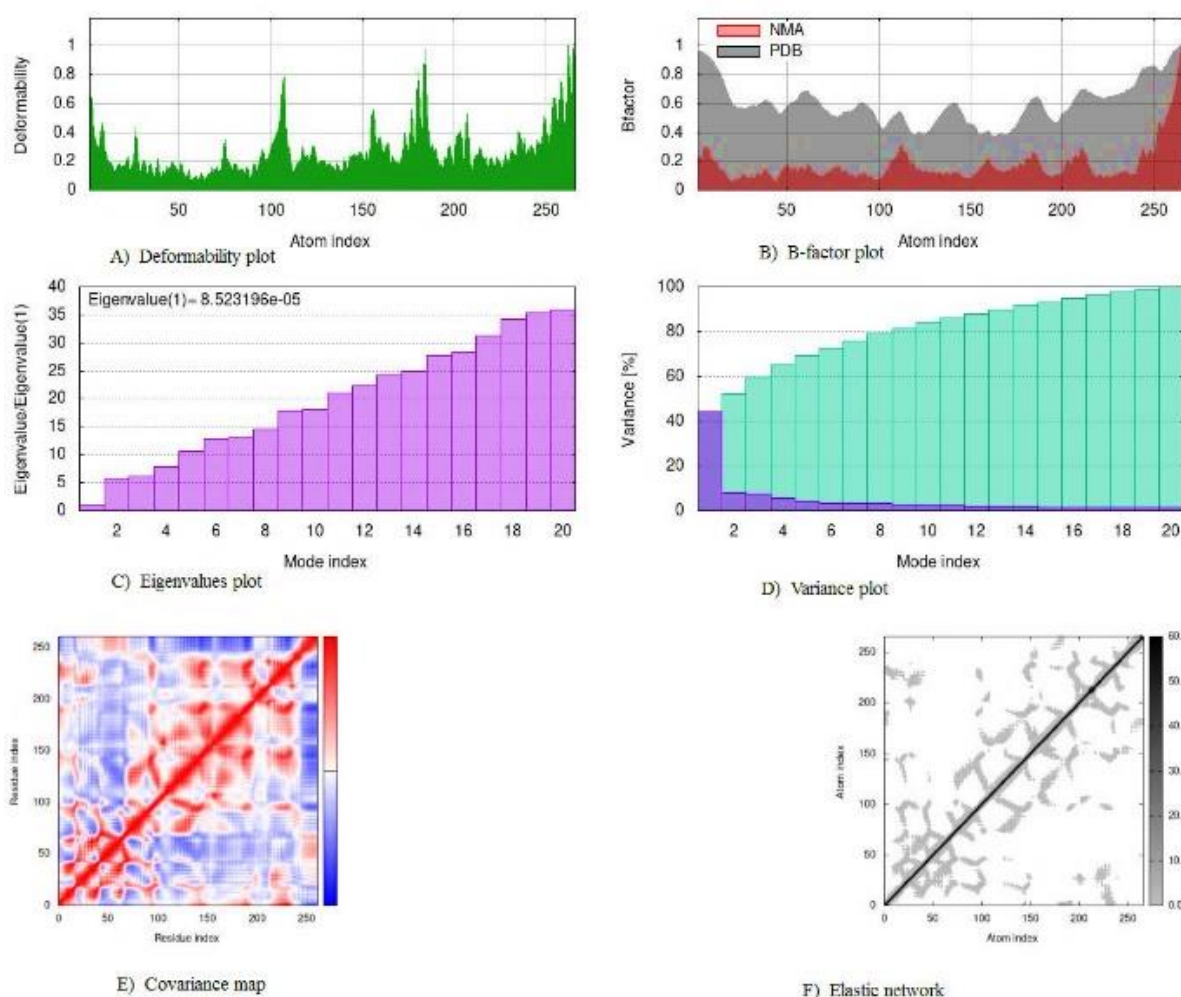


Figure 6. iMODs MD simulation results of HSD1 docked complex.

Table V shows the docking interactions of PPAR γ with the compounds showing the BA, K_i , HBs, HBIs, and other interactions. Compound IX (methyl 14-methylpentadecanoate) exhibited the least BA (-6.6 kcal/mol) and K_i (14 μ M) among all the compounds, followed by II (1,2-epoxyhexadecane) with BA and K_i of -6.2 kcal/mol and 28 μ M respectively. Although both compounds have the same numbers of HBs (4), Compound IX had more HBIs (11). The highest number of HBIs (13) was exhibited by Compound VII, while Compound VI had the highest HBs (5). Compounds IV, V, and I demonstrated the highest BA (-5.1 kcal/mol) and K_i (181 μ M), though Compound I had the highest HBs (4), while Compound VIII was the only compound that participated in CI.

The 2D and 3D interactions of PPAR γ with Compounds IX and II revealing the HBs with distances in angstrom and HBIs along with residues involved are shown in **Figure 7**. The HBs distances for Compound IX are between 2.85-3.35 \AA with

participating residues including His289, His323, Tyr473, and His449. For Compound II, HBs were only involved with His449 (2.85 Å) and Tyr473 (2.83 Å) – additionally, some of the residues in HBIs with both Compounds IX and II. **Figure 8** shows the RMSF of PPAR γ docked with Compounds IX and II. Compound IX's maximum (4.353 Å) fluctuation was observed at residue no. 427, the minimum (0.071 Å) fluctuation was observed at no. 388. The maximum (3.793 Å) fluctuation was observed for Compound II at residue no. 260, the minimum (0.090 Å) fluctuation was observed at residue no. 328. Furthermore, fluctuations were observed for Compounds IX and II at residues no. 207, 228, 244, 246, 260, 343, 359, 397, 427, 429, and 462. **Figure 9** displays the results of the iMODs MD simulations of the PPAR γ docked complex depicting the deformability, B-factor, eigenvalues, variance, covariance, and elastic network plots.

The PPAR γ , predominantly found in adipose tissues, acts as a nuclear receptor activating transcription factors associated with lipid and glucose homeostasis, improving dyslipidemia and insulin resistance⁴⁶. The antidiabetic agent thiazolidinediones is a typical example of a PPAR γ agonist, which, upon binding, promotes lipogenesis and suppresses lipolysis by insulin, thus increasing insulin sensitivity⁴⁷. In our study, the compounds were docked in the binding pocket of the PPAR γ agonist interacting with similar residues, including Ser289, His449, Tyr473, and His32345. Compound IX, which exhibited the lowest BA and K_i , participated in HBs interactions with the residues above surrounded by helix structures within the pocket. Similar interactions were observed for Compound II but with fewer HBs. The hydrophobic nature of these two compounds might contribute to their favorable interaction within this pocket compared to the other compounds, as observed in the ADME predictions. These compounds might act as agonists of PPAR γ , promoting its activity.

Moreover, the MD simulation revealed similar residue fluctuations for both compounds, supporting the impact of their binding on the conformation of the protein, with higher fluctuation observed for Compounds IX than II, thus more flexibility of the docked complex. Additionally, the superior number of HBs and HBIs exhibited by Compound IX is a sign of more potent and stable interaction than Compound II⁴⁸. This is further supported by the iMODs MD simulation showing low eigenvalue and higher deformability of the docked complex with an index close to 1.

Table V. Peroxisome proliferator-activated receptor γ (PPAR γ).

Compounds	BA (kcal/mol)	K_i (μ M)	HB	HBI	CI
IX	-6.6	14	4	11	-
II	-6.2	28	4	4	-
III	-6	40	3	12	-
VII	-6	40	1	13	-
X	-5.5	92	-	7	-
VI	-5.3	129	5	4	-
VIII	-5.3	129	2	7	His449
IV	-5.1	181	2	9	-
V	-5.1	181	2	9	-
I	-5.1	181	4	4	-

Note: BA = Binding affinity, K_i = Inhibition constant, HB = Hydrogen bonds, HBI = Hydrophobic interactions, CI = π -cation interaction

The docking interactions of AA with the compounds, including the BA, K_i , HB, HBI, and other interactions, are presented in **Table VI**. Compound X (methyl palmitate) had the least BA (-7.2 kcal/mol) and K_i (5 μ M), followed by Compound IX (methyl 14-methylpentadecanoate) with BA and K_i of -5.5 kcal/mol and 92 μ M respectively. Although both compounds have the same number of HBs (10), Compound IX had 2 HBs that absent in Compound IX. Compounds I and IV, having the same number of HBs (3), participated in PS with Tyr62. The highest BA (-5 kcal/mol), K_i (300 μ M), and HBs (4) were observed in Compound V, while the highest HBIs were seen in Compounds X and IX. The 2D and 3D interactions of AA with Compounds X and IX are shown in **Figure 10**, displaying the HBs bond distances, HBIs, and the residues involved. No HBs were observed for Compound X, though two were observed for Compound IX with Tyr151 (3.03 Å) and His201 (2.94 Å).

The RMSF profile of AA with Compound X and IX are shown in **Figure 11**. The maximum fluctuation (4.158 Å) for Compound X was observed at residue no. 224, while the minimum (0.047 Å) was seen at no. 14. A maximum (5.025 Å) fluctuation was observed at residue no. 144 for Compound IX, while the minimum (0.096 Å) was seen at no. 14. Additionally, fluctuations were seen at residues no. 7, 53, 73, 106, 122, 143, 152, 307, 350, 364, 460, 463, 471, 482, and 496. The iMODs MD simulation result of the AA docked complex is shown in **Figure 12**, displaying the deformability, B-factor, Eigenvalues, variance, covariance, and elastic network plots.

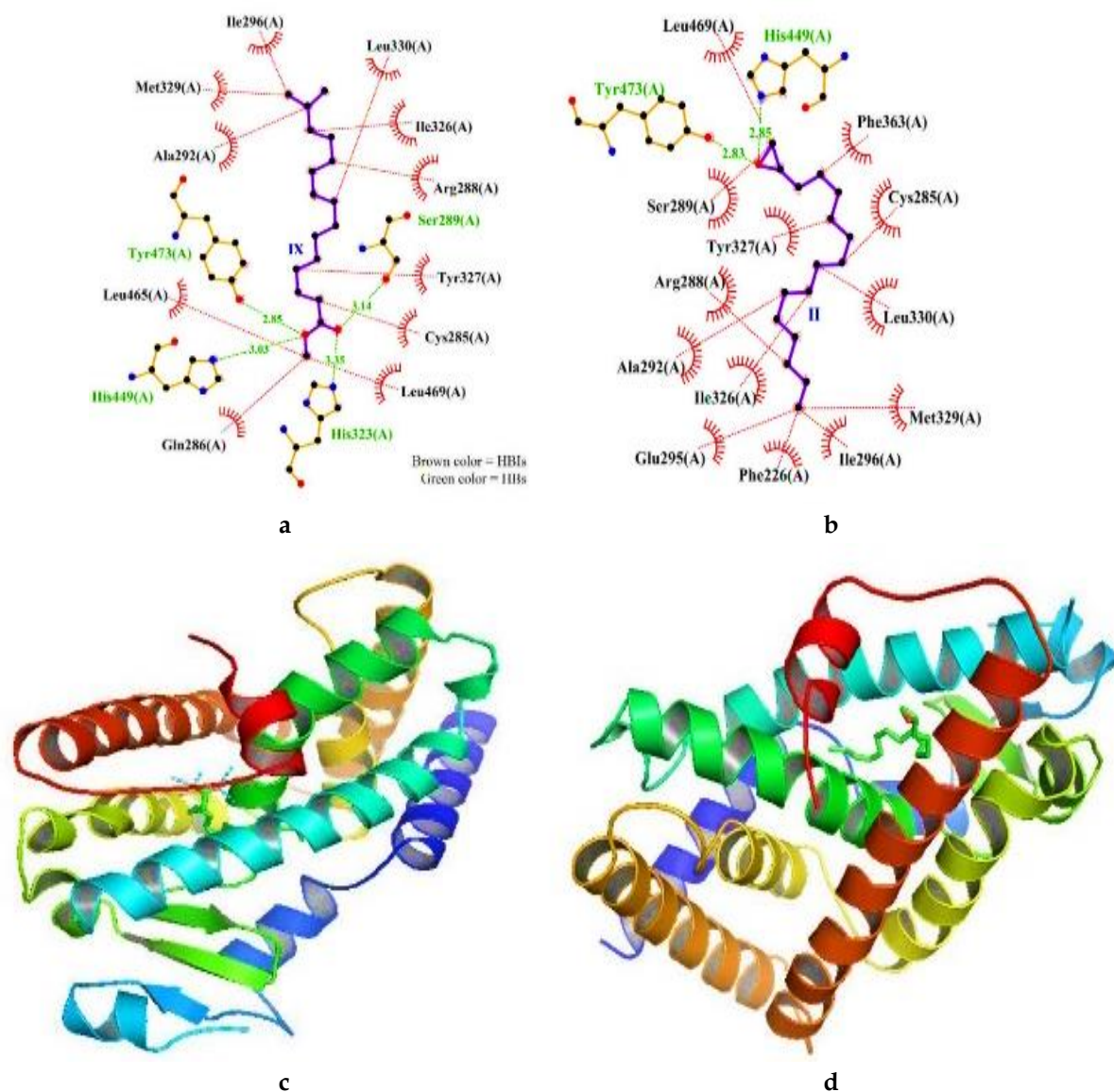


Figure 7. 2D and 3D interactions of PPAR γ with Compound IX and II. (a) 2D Compound IX; (b) 2D Compound II; (c) 3D Compound IX; and (d) Compound II.

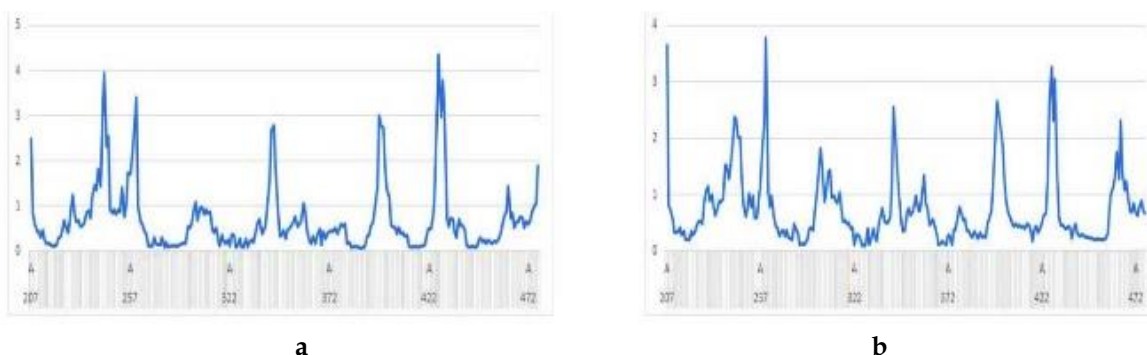


Figure 8. RMSF profile of PPAR γ with (a) Compound IX; and (b) II.

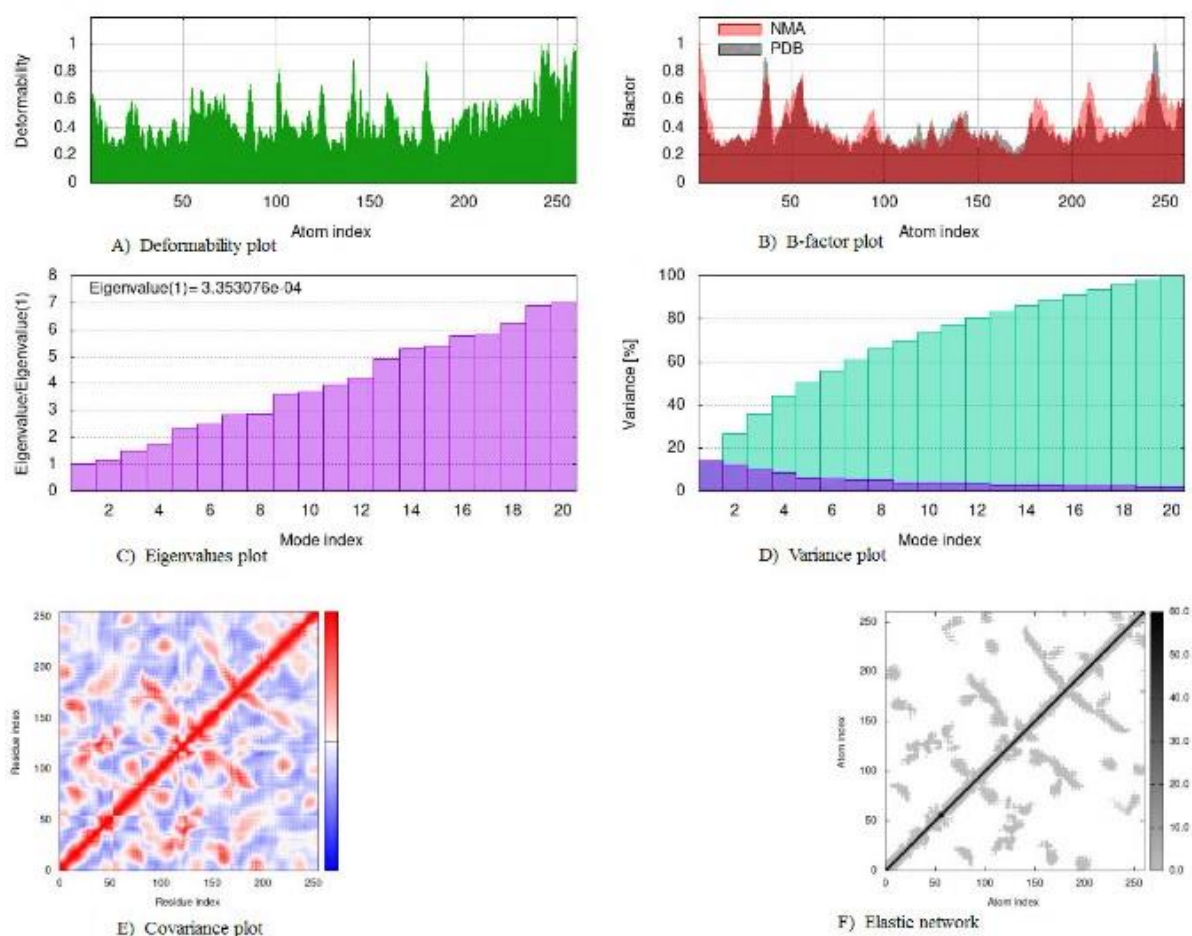


Figure 9. iMODs MD simulation results of PPAR γ docked complex.

α -amylase is a calcium-containing metalloenzyme that catalysis the hydrolysis of polysaccharides at the α -1,4 glycosidic bond into smaller molecules, including glucose and maltose, subsequently absorbed, leading to the elevation of blood glucose⁴⁹. Thus, a target of antidiabetic agents, specifically antihyperglycemic drugs, where inhibition of the enzyme prevents hyperglycemia. In our study, Compound X exhibited superior BA and K_i among the compounds, which might be attributed to the hydrophobic nature of the binding pocket, as up to 10 HBIs were formed with Compound X. The high number of HBIs might contribute to the stability of the complex formed with Compound X, though the B-factor plot shows some gaps in the NMA and PDB values of the complex, thus the residue fluctuations might prevent longer duration of action inhibiting the enzyme activity. Additionally, the RMSF values from the MD simulations show residues fluctuations of many residues, which might further suggest disruption of the original conformation, subsequently affecting the enzyme activity. Moreover, the MD simulation using iMODs sever also showed deformability of the enzyme structure, which might support the disruption of the enzyme activity due to the binding of Compound X.

Table VI. α -amylase (AA).

Compounds	BA (kcal/mol)	K_i (μ M)	HB	HBI	CI
X	-7.2	5	-	10	-
IX	-5.5	92	2	10	-
I	-5.1	181	3	3	Tyr62
IV	-5.1	181	3	4	Tyr62
II	-5	214	1	8	-
III	-5	214	1	9	-
VII	-5	214	1	8	-
VIII	-5	214	2	4	-
VI	-5	214	1	6	-
V	-4.8	300	4	3	-

Note: BA = Binding affinity, K_i = Inhibition constant, HB = Hydrogen bonds, HBI = Hydrophobic interactions, PS= π -stacking.

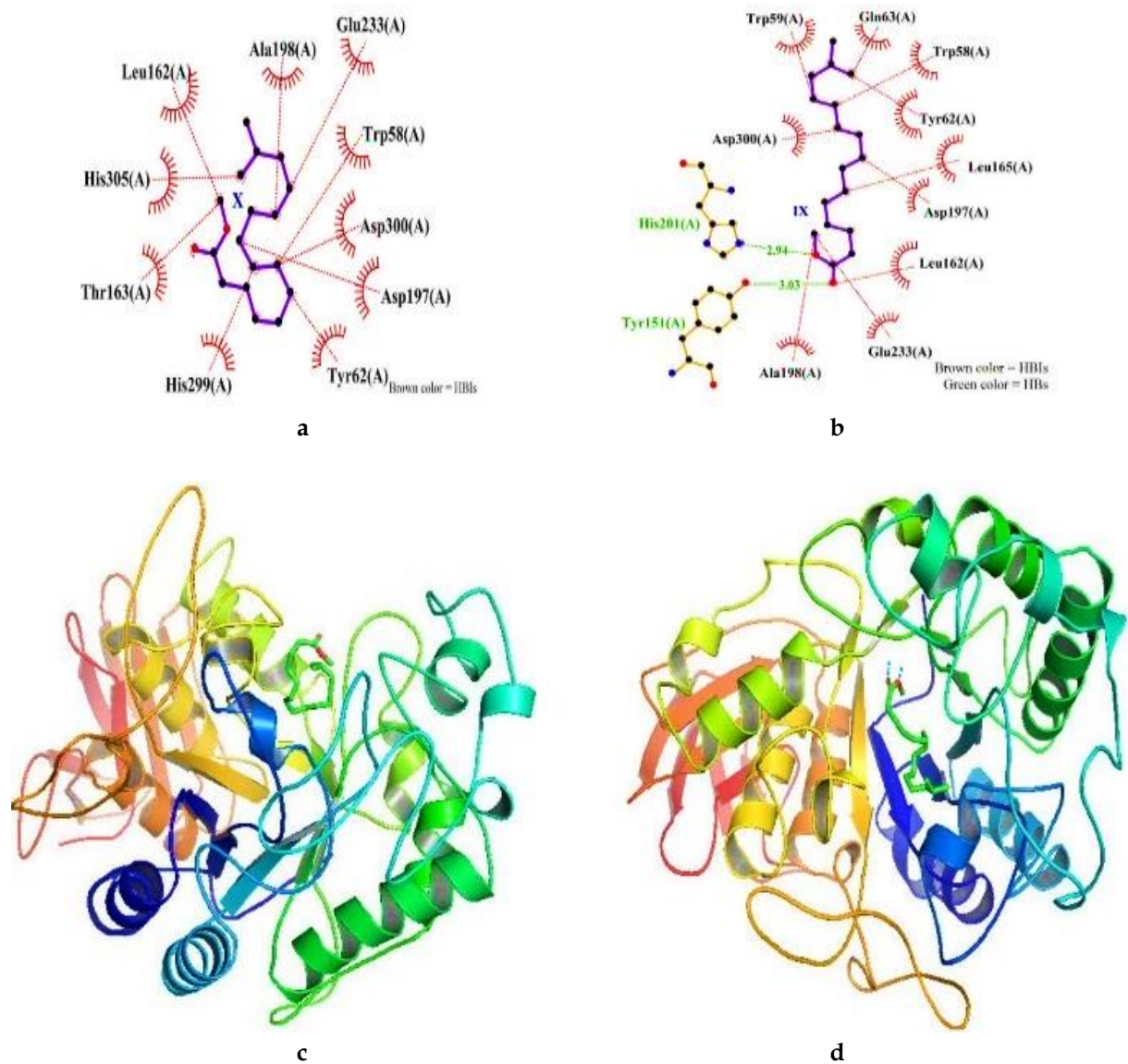


Figure 10. 2D and 3D interactions of AA with Compound X and IX. (a) 2D Compound X; (b) 2D Compound IX; (c) 3D Compound X; and (d) Compound IX.

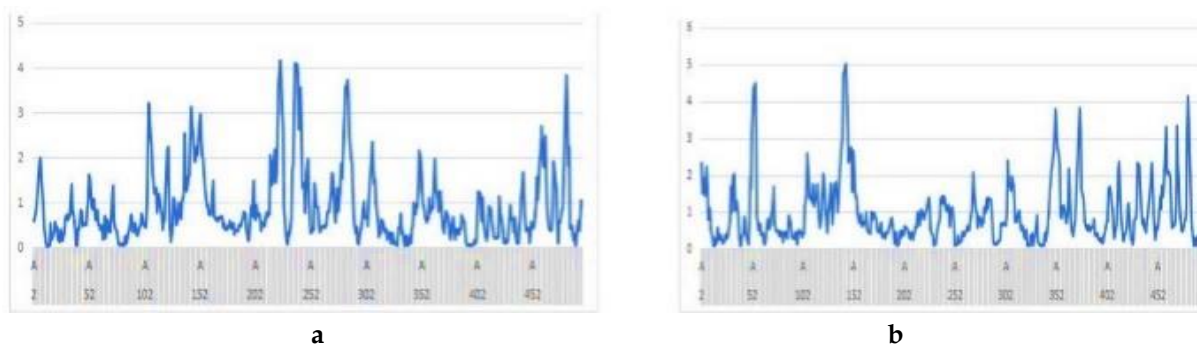


Figure 11. RMSF profile of AA with (a) Compound X; and (b) IX.

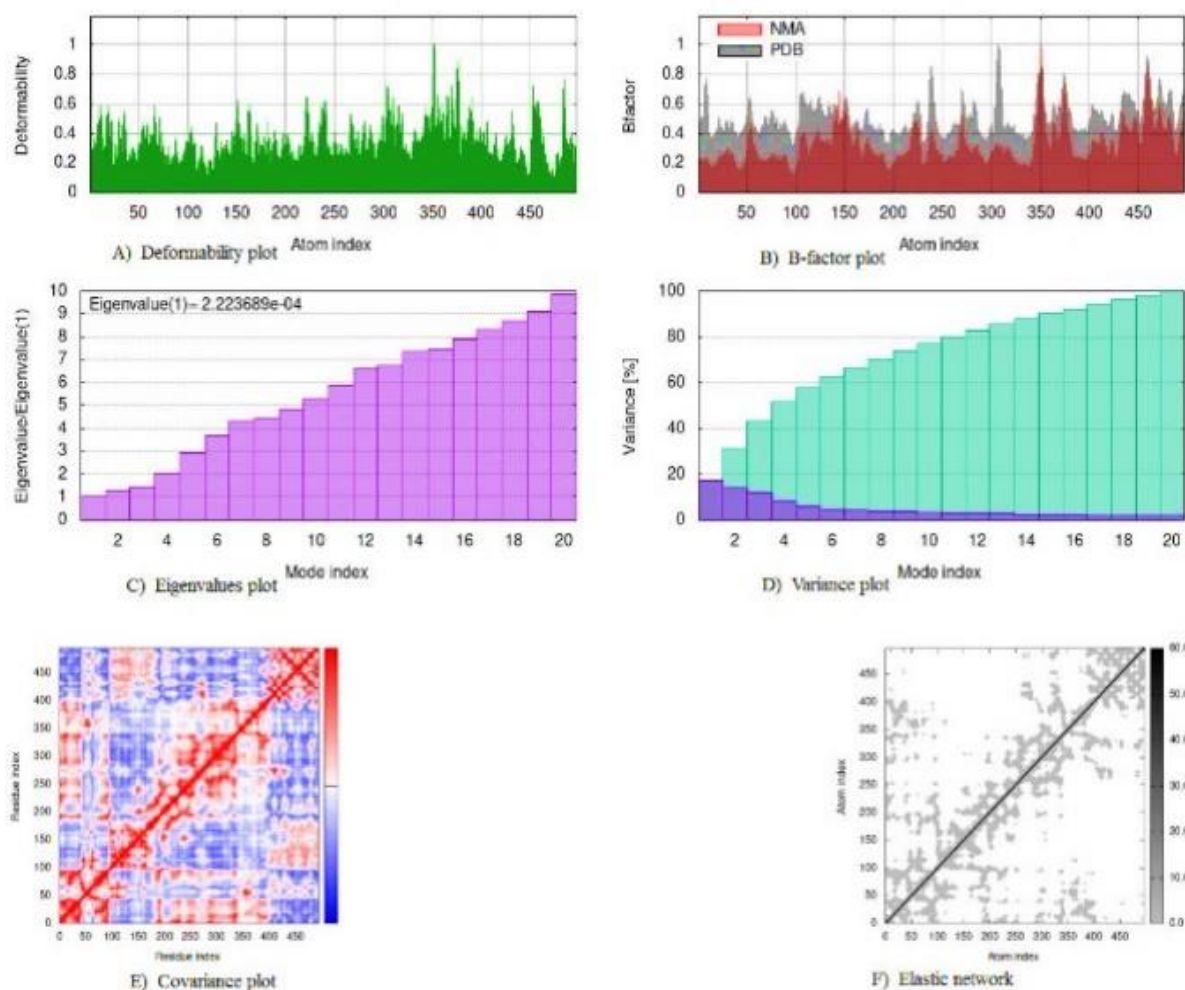


Figure 12. iMODs MD simulation results of AA docked complex.

Table VII presents the docking interactions of DPP-4 with the compounds, including the BA, K_i , and binding interactions. Compound I (1,2,4-benzotriol) demonstrated a slightly least BA (-5.8 kcal/mol) and K_i (55 μ M) followed by Compound VI (5-methyl-1H-pyrazole-3-carboxylic acid) with BA and K_i of -5.7 kcal/mol and 66 μ M respectively, though Compound VI had a superior number of HBIs (6) while Compound I had more HBs (3). The highest number of HBIs (10) were observed in Compounds X and IX, while the highest HBs were observed in Compound V. Additionally, Compound II exhibited the highest BA (-4.6 kcal/mol) and K_i (421 μ M) among all the compounds.

Figure 13 displays the 2D and 3D docked interactions of DPP-4 with Compounds I and VI, showing the HBs distances in \AA and HBIs with the residues involved. The HBs distance ranged from 2.83-3.25 \AA formed with Asp197 and His299 for Compound I, while Compound VI had only one HB with ASP197 (2.88 \AA). **Figure 14** presents the RMSF profile of Compounds I and IV interactions. The maximum (4.368 \AA) fluctuation for Compound I was observed at residue no. 148, while the minimum (0.051 \AA) was observed at residue 302. Compound VI's maximum (4.326 \AA) fluctuation was observed at residue no. 742, while the minimum (0.083 \AA) was at residue 469. Additionally, similar fluctuations for both compounds were observed at residue no. 38, 261, 400, 438, 450, 520, 535, 645, 678, 743, and 766. The iMODs MD simulation results of the DPP-4 docked complex show the deformability, B-factor, eigenvalues, variance, covariance, and elastic network plots. The iMODs MD simulation result of the DPP-4 docked complex is shown in **Figure 15**.

DPP-4 is a critical enzyme in maintaining glucose homeostasis via proteolytic cleavage of the incretin hormone GLP-1 and gastric inhibitory peptide (GIP), contributing to glucose homeostasis and regulating activity. Thus, this enzyme serves as a target of antihyperglycemic agents via its inhibition. The proteolytic activity of these enzymes makes them vital in regulating other peptides associated with insulin sensitivity⁵⁰. In our study, Compounds I and VI docked in the binding pocket of vildagliptin exhibited similar interaction, though Compound I exhibited superior interaction with more HBs and HBIs,

demonstrating binding strength and stability compared to Compound VI. The binding of these compounds might inhibit the enzyme's activity, as in the case of vildagliptin, thereby prolonging insulin action and preventing hyperglycemia. Moreover, the MD simulation points to the docked complex's flexibility, deformability, and stability, which further suggests the disruption of the enzyme activity with the RMSF profile, showing multiple fluctuations of the enzyme residues. At the same time, the eigenvalue was observed to be low.

Table VII. Dipeptidyl peptidase IV (DPP-4).

Compounds	BA (kcal/mol)	K _i (μM)	HB	HBI	CI
I	-5.8	55	3	3	3
VI	-5.7	66	1	6	6
IV	-5.3	129	3	4	4
X	-5.3	129	-	10	10
VIII	-5.2	153	2	4	4
IX	-5.1	181	2	10	10
III	-5.1	181	1	9	9
V	-4.8	300	4	3	3
VII	-4.8	300	1	8	8
II	-4.6	421	1	8	8

Note: BA = Binding affinity, K_i = Inhibition constant, HB = Hydrogen bonds, HBI = Hydrophobic interactions.

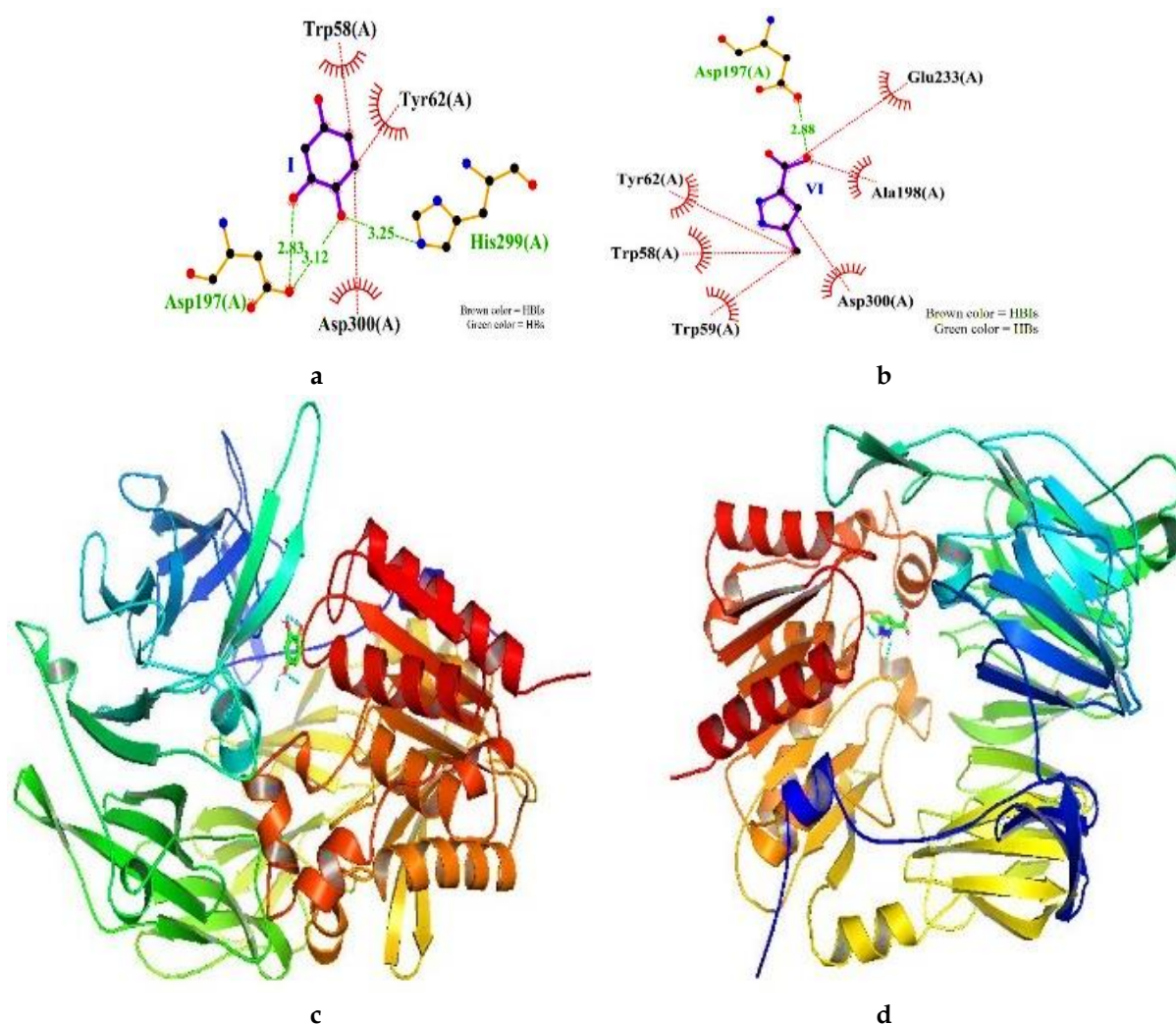


Figure 13. 2D and 3D interactions of DPP-4 with Compound I and VI. (a) 2D Compound I; (b) 2D Compound VI; (c) 3D Compound I; and (d) Compound VI.

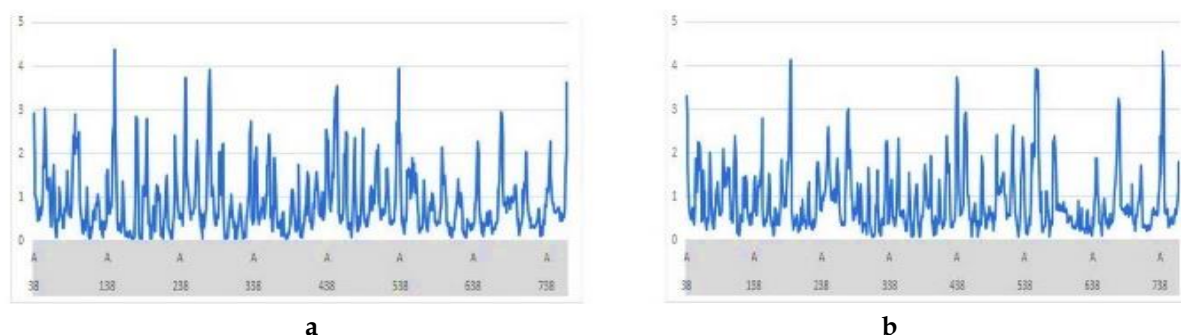


Figure 14. RMSF profile of DPP-4 with (a) Compound I; and (b) VI.

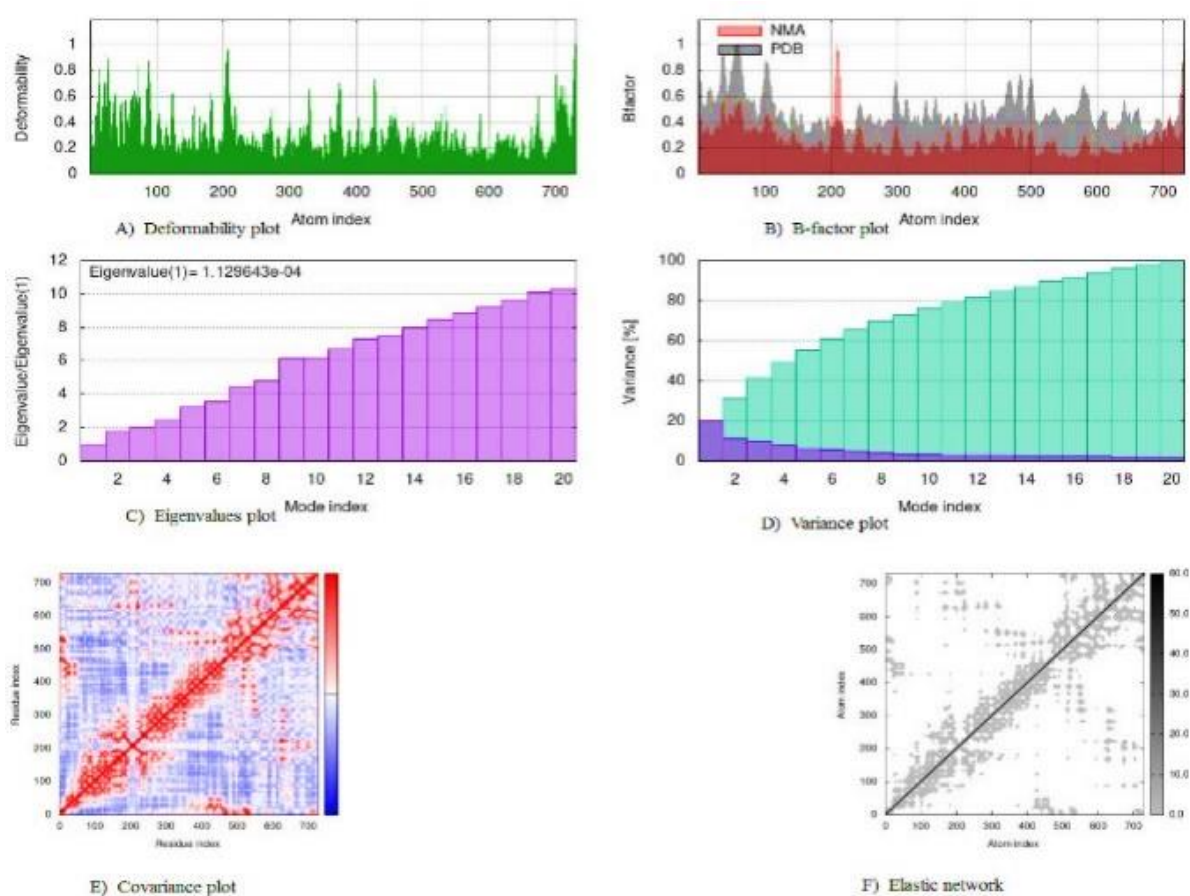


Figure 15. iMODs MD simulation results of DPP-4 docked complex.

The docking interactions of GLP1 with the compounds showing the BA, K_i , and other binding interactions are presented in **Table VIII**. Among the compounds, the least BA (-8.7) and K_i ($4.1 \times 10^{-1} \mu\text{M}$) was exhibited by Compound X (methyl palmitate), followed by IX (methyl 14-methylpentadecanoate) with BA and K_i of -6.3 kcal/mol and 24 μM respectively. Although no HB was observed for Compound X, Compound IX had 1 HB with fewer HBIs (6) than Compound X (8). Furthermore, PS interaction with Trp33 was observed for Compound IX. Compounds III, IV, V, and VIII had the highest HBs (2), while Compounds VII and III had the highest HBIs. Compound VIII exhibited the highest BA (-4.7 kcal/mol) and K_i (μM) among all the compounds, though it participated in PS interaction with Arg380.

The 2D and 3D docking interactions of GLP1 with Compounds X and IX, showing the HB interaction with distance and HBIs, are presented in **Figure 16**. Although no HBs were formed for Compound X, Compound IX participated in HB formation with Gln221 with a distance of 2.98 Å— Additionally, both compounds interacted with similar residues forming HBIs. The RMSF profile of GLP1 docked with Compounds X and IX showing the fluctuations of the residues are shown in **Figure 17**. For Compound X, a maximum fluctuation of 5.014 Å was observed at residue no. 338, while a minimum (0.079

Å) fluctuation was observed at residue no. 237. Compound IX had a maximum (4.012 Å) fluctuation at residue no. 92 while the minimum (0.099 Å) was seen at no. 240. However, similar fluctuations were observed for both compounds at residue no. 58, 108, 117, 135, 171, 295, 343, and 421. The iMODs MD simulation results of GLP1 docked complex showing the deformability, B-factor, eigenvalues, variance, covariance, and elastic network plots are presented in **Figure 18**.

Glucagon-like peptide 1 receptor is an incretin hormone that stimulates insulin secretion and suppresses glucagon secretion, thus regulating postprandial glucose influx. Additionally, GLP1 contributes to the control of food intake and appetite. Thus, this enzyme is a target of antihyperglycemic agents preventing postprandial hyperglycemia⁵¹. Here, the GLP1 receptor is the target of an agonist that mimics the effects of GLP1, offering more advantage over other antihyperglycemic agents without the risk of hypoglycemia⁸. In our study, the compounds were docked with GLP1 receptors where Compound X exhibited the lowest BA and K_i stabilized with HBs, though no HBs were observed. The binding of Compound X to the receptor might mimic the activity of GLP1 acting as an agonist to the receptor, thereby prompting the GLP1 effect mentioned earlier. The MD simulation further revealed many residue fluctuations within the protein structure, depicting the flexibility of the complex, with iMODs simulation showing a lot of deformability and mobility within the complex structure. Thus, it might translate to forming a stable and flexible complex with good mobility, subsequently stimulating the GLP1 receptor.

Table VIII. Glucagon-like Peptide-1 Receptor (GLP1).

Compounds	BA (kcal/mol)	K_i (μ M)	HB	HBI	CI
X	-8.7	4.1×10^{11}	-	8	-
IX	-6.3	24	1	6	Trp33
VII	-6.1	33	1	9	-
II	-5.8	55	1	7	-
III	-5.5	92	2	9	-
IV	-4.9	254	2	3	-
I	-4.8	300	1	8	-
VI	-4.8	300	1	6	-
V	-4.7	356	2	6	-
VIII	-4.7	356	2	5	Arg380

Note: BA = Binding affinity, K_i = Inhibition constant, HB = Hydrogen bonds, HBI = Hydrophobic interactions, PS= π -stacking.

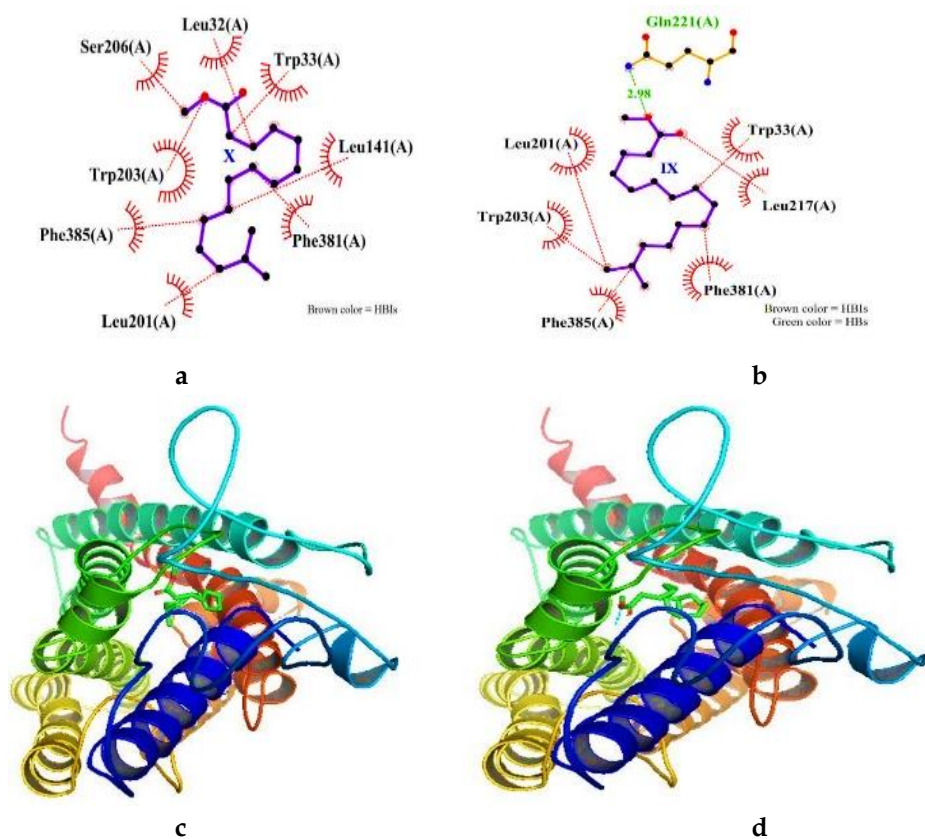


Figure 16. 2D and 3D interactions of GLP1 with Compound X and IX. (a) 2D Compound X; (b) 2D Compound IX; (c) 3D Compound X; and (d) Compound IX.

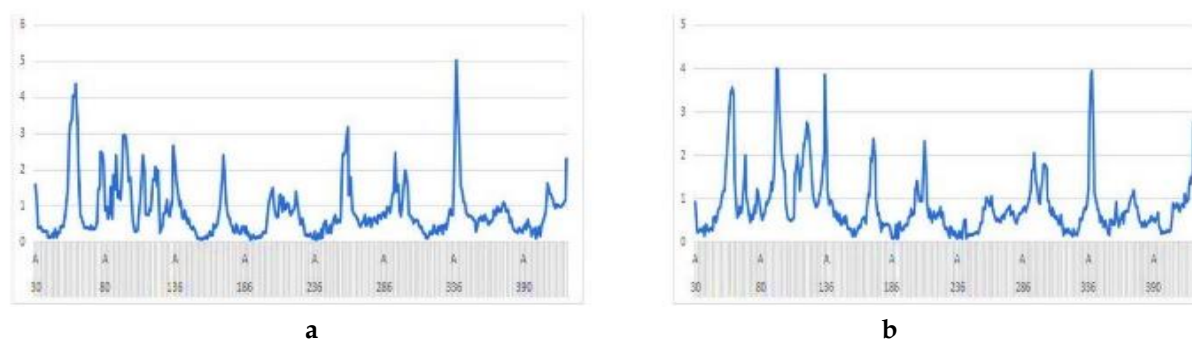


Figure 17. RMSF profile of GLP1 with (a) Compound X; and (b) IX.

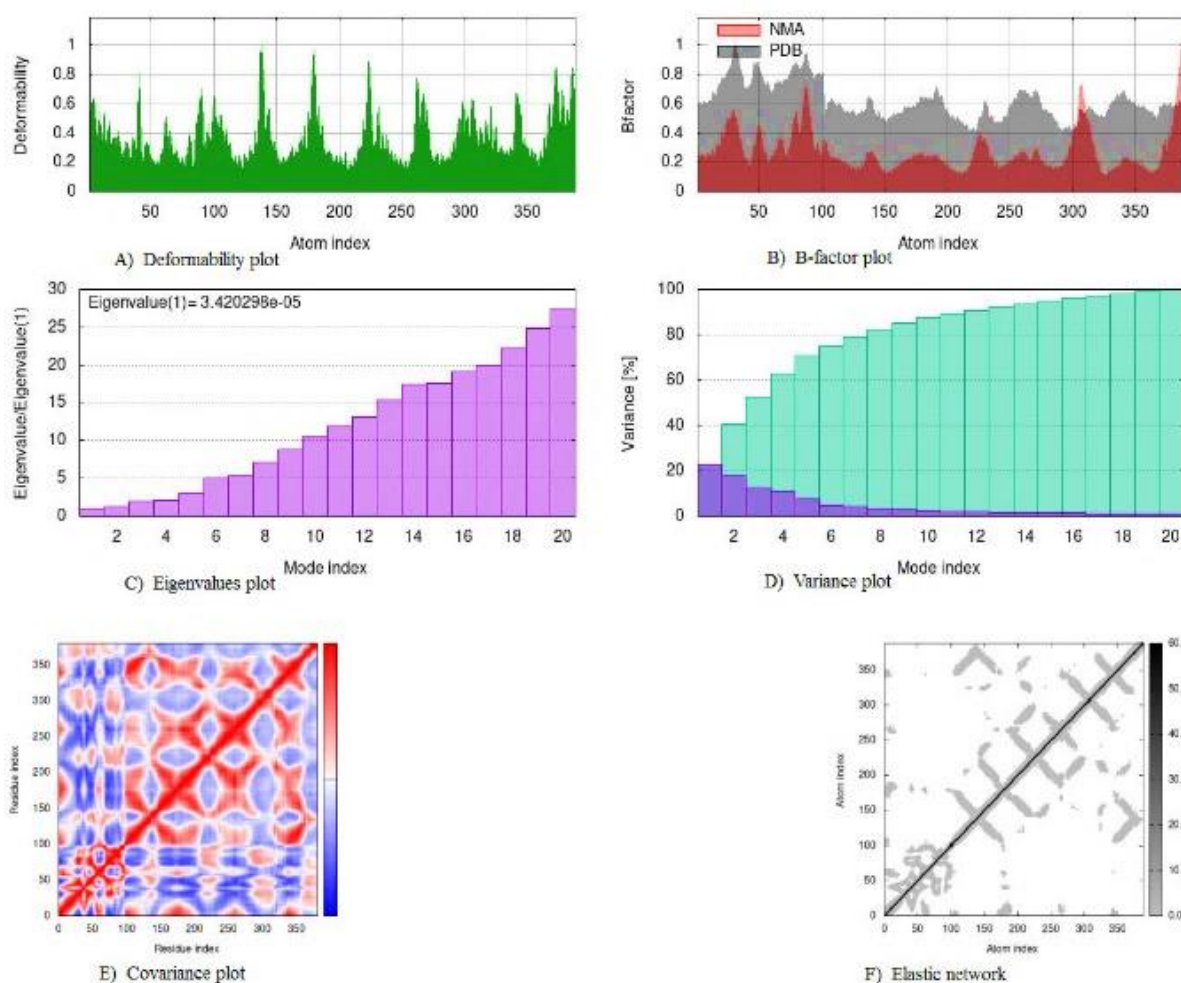


Figure 18. iMODs MD simulation results of GLP1 docked complex.

Table IX presents the docking interactions of SGLT2 with the compounds showing the BA, K_i , and binding interactions. The lowest BA (-7.6 kcal/mol) and K_i (3 μ M) were exhibited by Compound X (methyl palmitate) followed by Compound IX (methyl 14-methylpentadecanoate) with BA and K_i of -6.6 kcal/mol and 14 μ M respectively. However, Compound IX had more HBIs (14) among all the compounds, and HB was absent in Compound X. Among the compounds, the highest BA (-5.6 kcal/mol), K_i (78 μ M), and number of HB (5) were seen in Compound V. Additionally, Compounds I and VIII participated in PS interactions with Arg290.

Figure 19 shows the 2D and 3D docking interactions of SGLT2 with Compounds X and IX, depicting the HBs distances, HBIs, and the residues involved. Although no HBs were observed for Compound X, the residues involved in HBIs for Compound X were similar to those for Compound IX, which participated in HB interaction with Trp291 (3.01 Å). **Figure 20** presents the RMSF profile of SGLT2 with Compounds X and IX, revealing the residue fluctuations of the docked complex.

The maximum (4.24 Å) fluctuation observed for Compound X was at residue no. 254, while the minimum (0.043 Å) was observed at no. 317. The maximum (5.37 Å) fluctuation for Compound IX was at residue no. 247, while the minimum (0.056 Å) was at no. 390. Furthermore, similar fluctuations were observed for both compounds at residues no. 21, 49, 92, 136, 245, 246, 270, 416, 448, and 551. **Figure 21** shows the iMODs MD simulation results of the SGLT2 docked complex depicting the deformability, B-factor, eigenvalues, variance, covariance, and elastic network plots.

Sodium-glucose cotransporter-2 is a cotransporter located in the proximal tubule involved in the renal reabsorption of up to 80% of glucose from the glomerulus⁵². Therefore, SGLT2 inhibitors inhibit the reabsorption of filtered glucose from the kidney, decreasing the circulating glucose level independent of insulin⁵³. Compound X demonstrated superiority in interacting with SGLT2 with many HBIs, which might point to stability rather than strength, as no HBs were observed. This compound might interrupt and inhibit SGLT2, considering the MD simulation results, which show the stability of the complex formed accompanied by few residue fluctuations and a low deformability index of less than 0.8. Additionally, the B-factor plot further supports the postulated stability of the complex as there were few peaks formed by the complex, whereas the deformability index shows the flexibility of the complex, though the low eigenvalue observed might translate to weakness in the complex.

Table IX. Sodium-Glucose Cotransporter 2 (SGLT2).

Compounds	BA (kcal/mol)	K _i (μM)	HB	HBI	CI
X	-7.5	3	-	11	-
IX	-6.6	14	1	14	-
III	-6.3	24	4	14	-
II	-6.2	28	1	11	-
IV	-6	40	3	6	-
VII	-6	40	1	10	-
I	-5.9	47	3	6	Tyr290
VI	-5.9	47	2	7	-
VIII	-5.9	47	3	5	Tyr290
V	-5.6	78	5	2	-

Note: BA = Binding affinity, K_i = Inhibition constant, HB = Hydrogen bonds, HBI = Hydrophobic interactions, PS = π-π-stacking.

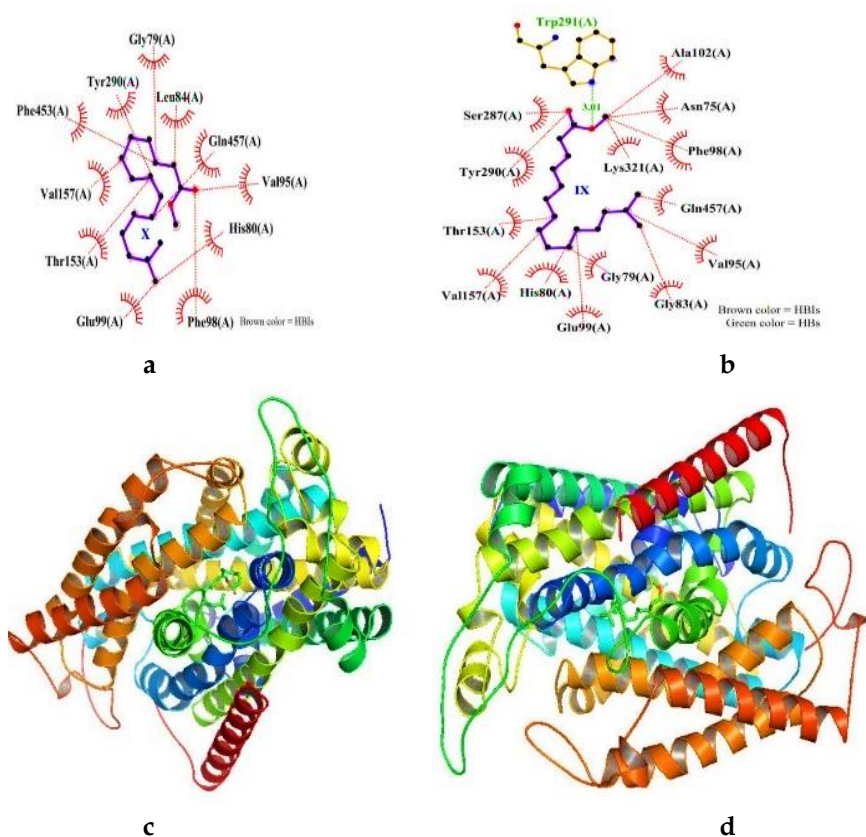


Figure 19. 2D and 3D interactions of SGLT2 with Compound X and IX. (a) 2D Compound X; (b) 2D Compound IX; (c) 3D Compound X; and (d) Compound IX.

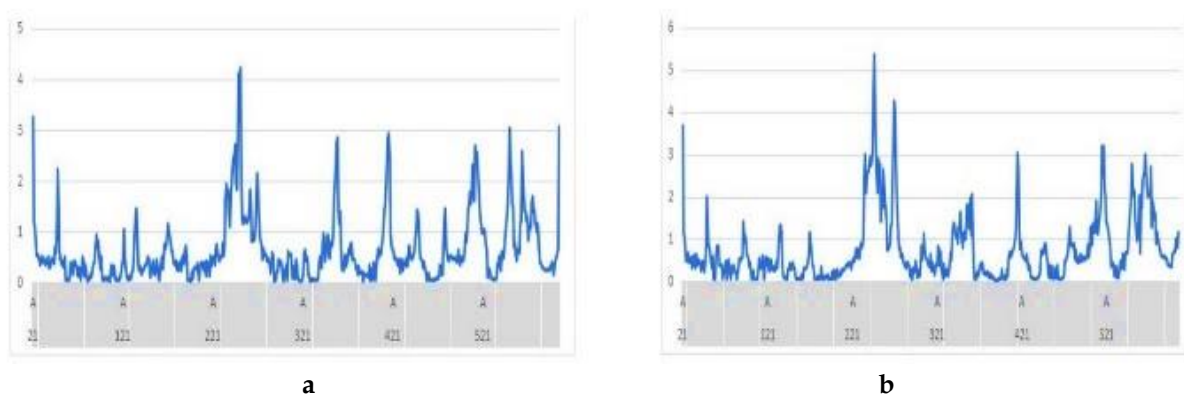


Figure 20. RMSF profile of SGLT2 with (a) Compound X; and (b) IX.

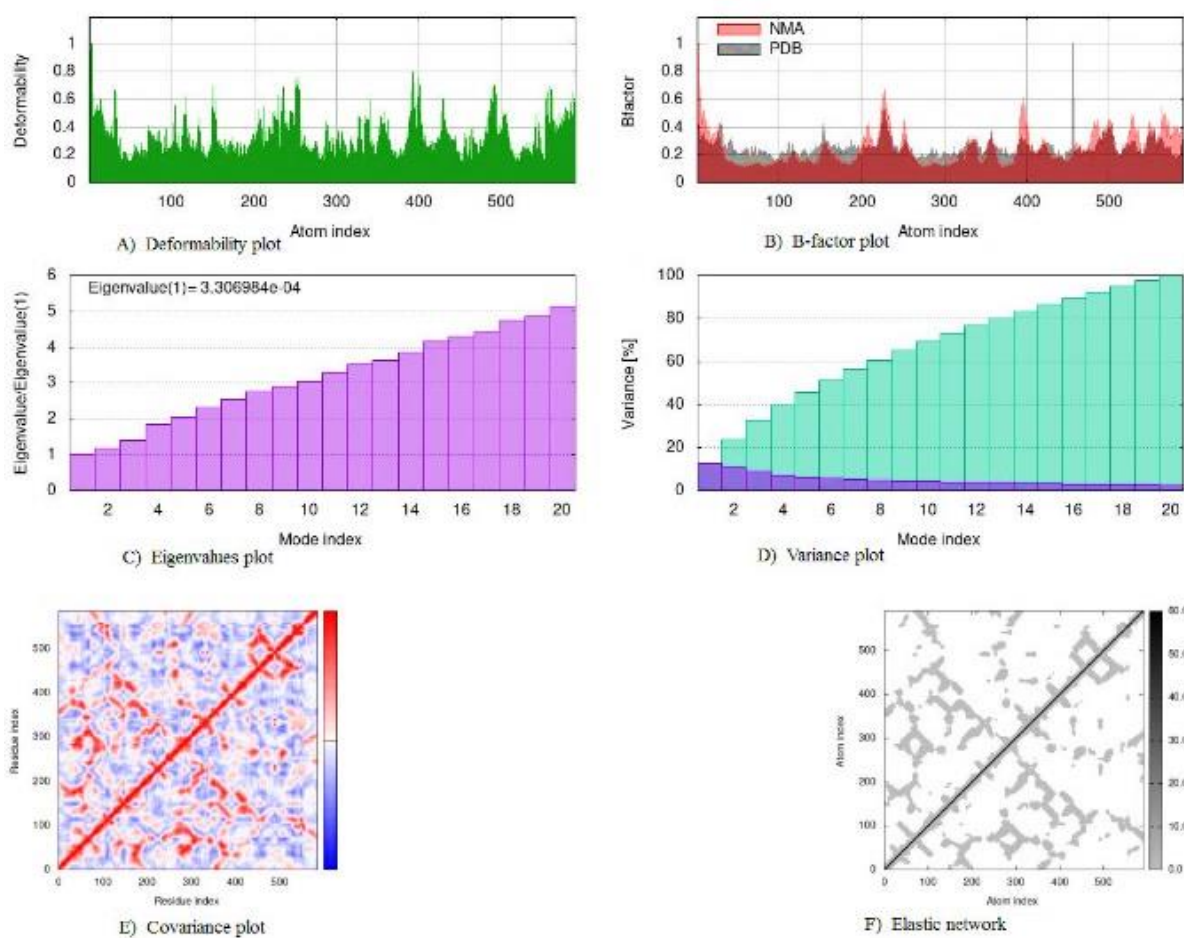


Figure 21. iMODs MD simulation results of SGLT2 docked complex.

The docking interactions of AG with the compounds showing the BA, K_i , and binding interactions are presented in **Table X**. Among the compounds, Compound VI (5-methyl-1H-pyrazole-3-carboxylic acid) had the least BA (-6 kcal/mol) and K_i (40 μ M) followed by Compound X (methyl palmitate) with BA and K_i of -5.8 kcal/mol and 55 μ M respectively. Moreover, Compound VI had the highest numbers of HBIs (9) and HBs (2), absent in Compound X. Compounds I, IV, II, and V were the compounds with the highest number of HBs (3), while Compound VII had the highest HBIs (12). The highest BA (-4.9 kcal/mol) and K_i (254 μ M) were seen in Compound V.

The 2D and 3D docking interactions of AG with Compounds VI and X, showing the HBs distances, HBIs, and the residues involved, are presented in **Figure 22**. For Compound VI, HBs were formed with His626 and Asp357 with distances of 3.01 and 2.95 Å, respectively, though absent in Compound X. However, there were HBIs with similar residues for both

Compounds VI and X. **Figure 23** shows the RMSF profile of AG with Compounds VI and X depicting the fluctuating residues of the docked complex. The maximum (5.317 Å) fluctuation for Compound VI was observed at residue no. 181, while the minimum (0.038 Å) was at no. 93. For Compound X, the maximum (4.63 Å) fluctuation was seen at residue no. 137, whereas the minimum (0.054 Å) was at no. 581. However, a similar fluctuation was observed for both compounds at residue no. 56, 108, 373, 406, 462, 500, 685, 710, and 805. The iMODs MD simulation results of the AG docked complex are shown in **Figure 24**, showing the deformability, B-factor, eigenvalues, variance, covariance, and elastic network plots.

α -glucosidase found in the brush borders of the small intestine contributes to the digestion of carbohydrates, selectively hydrolyzing the 1 \rightarrow 4-linked α -glucose residues, releasing single glucose molecules in the process leading to elevation of blood glucose. α -glucosidase inhibitors act by competitively inhibiting the action of AG, delaying the digestion of carbohydrates, reducing glucose absorption, and preventing hyperglycemia⁵⁴. In our study, Compound VI demonstrated superior interaction with AG, evidenced by the low BA and K_i values. MD simulation shows a lot of residue fluctuation of the enzyme docked complex, with many hinge regions within the complex reflecting on the flexibility of the complex. Furthermore, the deformability and mobility of the complex further suggest conformation change within the complex. The result suggests that the binding of this compound might inhibit the enzyme's activity, preventing the substrate's attachment.

Table X. α -glucosidase (AG).

Compounds	BA (kcal/mol)	K_i (μ M)	HB	HBI
VI	-6	40	2	9
X	-5.8	55	-	8
I	-5.7	66	3	6
IV	-5.7	66	3	8
II	-5.5	92	-	11
VIII	-5.5	92	2	7
VII	-5.4	109	1	12
IX	-5.4	109	1	9
III	-5.2	153	3	7
V	-4.9	254	3	7

Note: BA = Binding affinity, K_i = Inhibition constant, HB = Hydrogen bonds, HBI = Hydrophobic interactions.

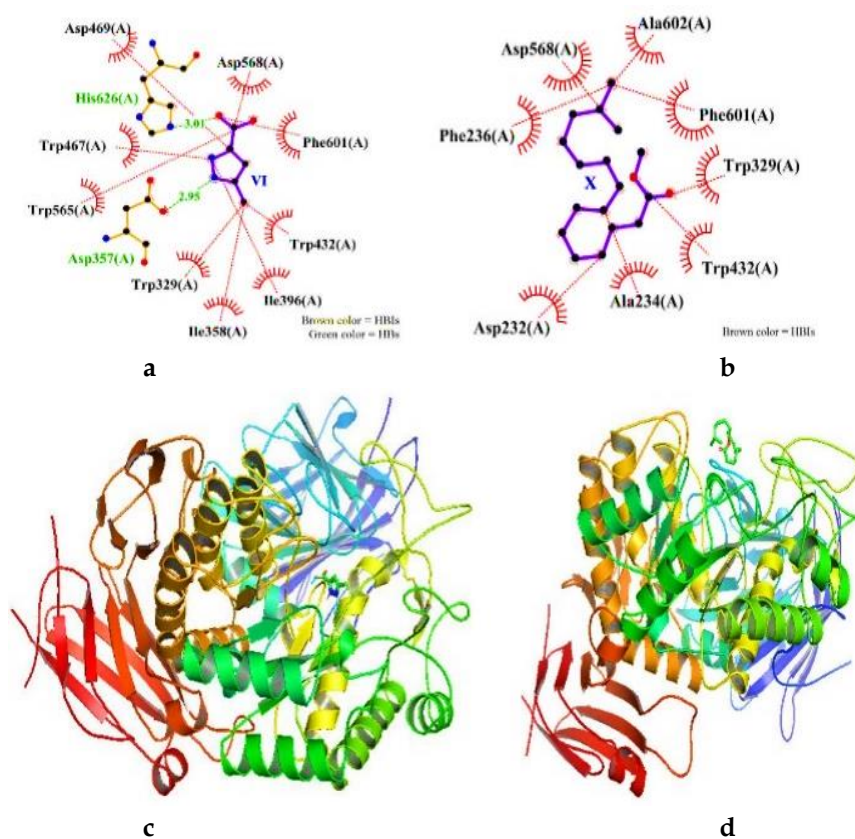


Figure 22. 2D and 3D interactions of AG with Compound VI and X. (a) 2D Compound VI; (b) 2D Compound X; (c) 3D Compound VI; and (d) Compound X.

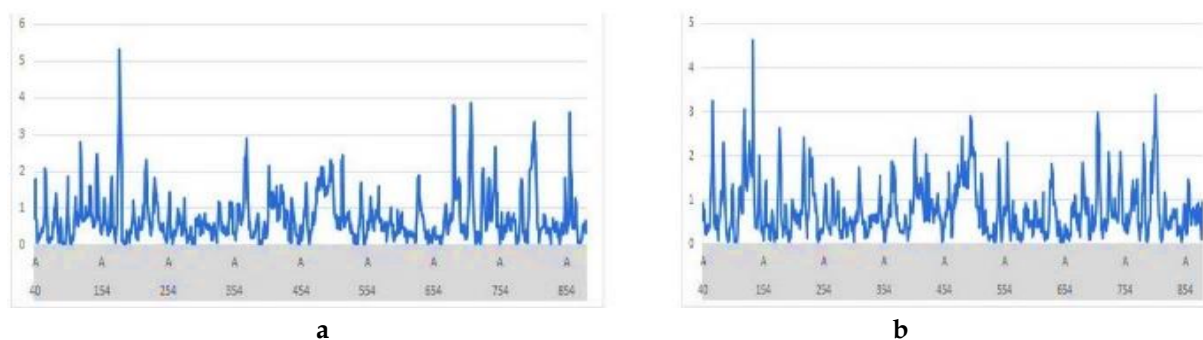


Figure 23. RMSF profile of AG with (a) Compound VI; and (b) X.

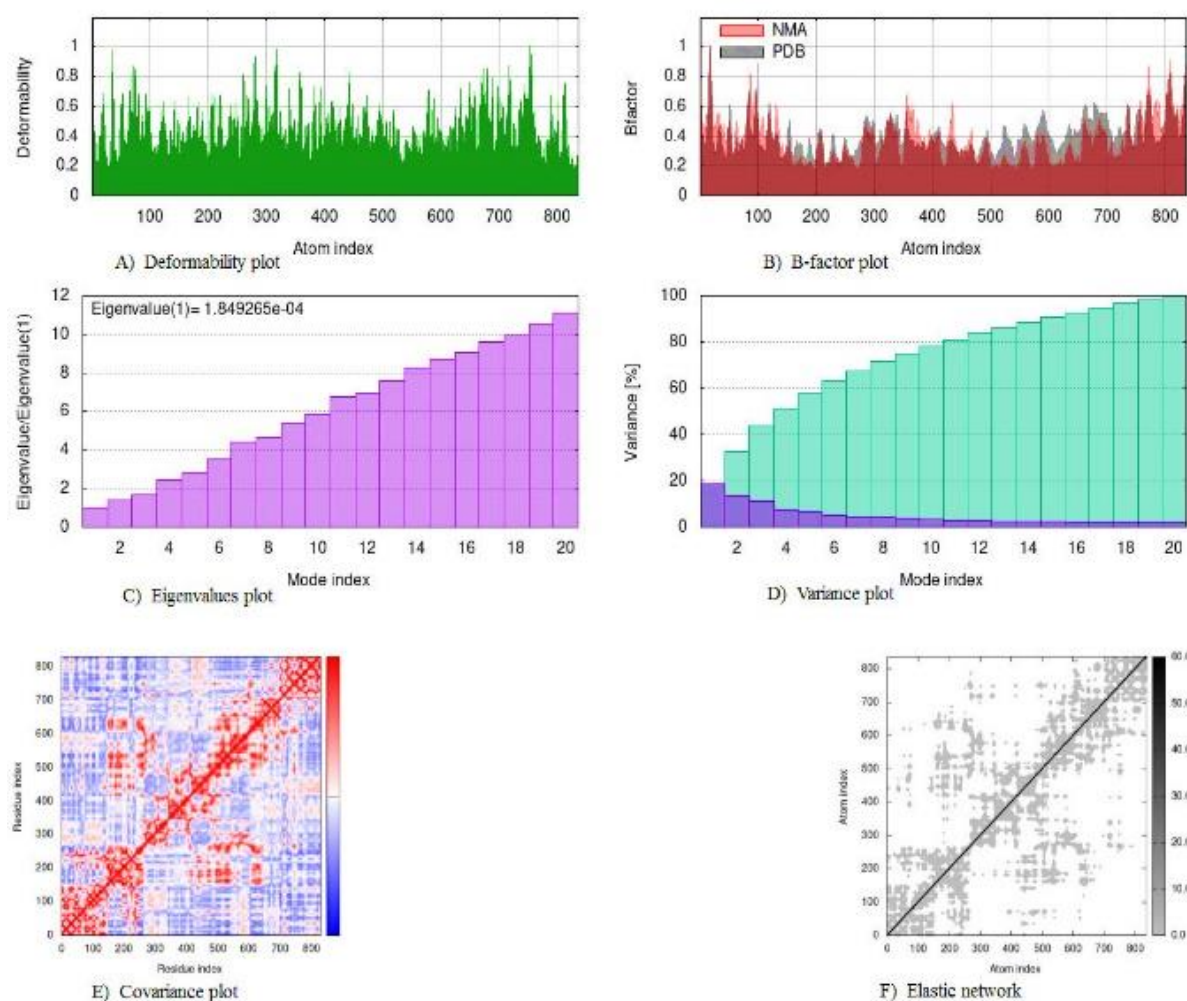


Figure 24. iMODs MD simulation results of AG docked complex.

Eigenvalue is a measure of motion stiffness of the docked complex reflecting the energy required to deform the structure; directly proportional to the ease of deformability of the complex³⁵. As previously mentioned, all of the docked complexes in our study exhibited ease of deformability with low eigenvalues. The low eigenvalues and deformability point to good flexibility and stability of the docked complex molecular motion. All the docked complexes in our study exhibited low eigenvalues, with GLP1, HSD1, and AA among the lowest (**Table XI**).

Table XI. Eigenvalues of iMODs MD Simulations.

Target protein	Eigenvalues
Protein tyrosine phosphatase 1B (PTP1B)	3.66×10^4
11- β -hydroxysteroid dehydrogenase (HSD1)	8.52×10^5
Peroxisome proliferator-activated receptor γ (PPAR γ)	3.35×10^4
α -amylase (AA)	2.22×10^4
Dipeptidyl peptidase IV (DPP-4)	1.30×10^4
Glucagon-like peptide 1 receptor (GLP1)	3.42×10^5
Sodium-glucose cotransporter-2 (SGLT2)	3.31×10^4
α -glucosidase (AG)	1.85×10^4

The drug-likeness parameters and synthetic accessibility of the compounds are presented in **Table XII**, showing the MW, TPSA, ESOL, Fraction Csp3, rotatable bonds, and bioavailability score. The MW of the compounds ranges from 126.11 to 270.45 g/mol, with Compounds I, V, VI, and VIII having the while Compounds IX and X the highest. The TPSA of all the compounds ranged from 12.53 to 65.98 Å², with Compound II busting the least while Compound VI the highest. The ESOL values ranged from -5.18 to -0.54, with Compound X exhibiting the least while Compound V was the highest. The number of rotatable bonds for the compounds ranged from 0 to 15, with Compounds I and VIII having none while Compounds III and X have 15. All the compounds had a bioavailability score 0.55 except Compound VI (0.85). The synthetic accessibility of the compounds ranged from 1 to 3.01, with Compound I being the least while Compound III was the highest. Additionally, Compounds IX and X had the same value for synthetic accessibility.

Drug likeness techniques are employed to predict the possibility of a compound being an oral drug by assessing its physicochemical properties to predict its bioavailability and oral drug potential³⁶. The abbot bioavailability is employed to predict the probability of a compound having at least 10% oral bioavailability in rats or measurable in the Caco-2 cell line permeability experiment⁵⁵. The Caco-2 model is applied to predict the human intestinal absorption of drugs with the consideration of lipophilicity ($-0.7 < XLOGP3 < 5.0$), molecular weight (MW) ($150 \text{ g mol}^{-1} < MW < 500 \text{ g mol}^{-1}$), polarity ($20 \text{ \AA}^2 < TPSA < 130 \text{ \AA}^2$), solubility ($0 < \log S \text{ (ESOL)} < 6$), saturation ($0.25 < \text{Fraction Csp3} < 1$) and flexibility ($0 < \text{of rotatable bonds} < 9$). This rule quantitatively defines the compound into probability classes of four: 11, 17, 55, and 85%, with 55% being the accepted class, depicting the passing of the rule of five^{55,56}. In our study, all the compounds were predicted to have a bioavailability score of 55%, except Compound VI, with a bioavailability score of 85%. Furthermore, the complexity of the compound structures was assessed by the synthetic accessibility score to ascertain structural complexity and ease of synthesis. The synthetic accessibility score is graded from 1 (the easiest to synthesize) to 10 (very difficult to synthesize)⁵⁷. In our study, the synthetic accessibility score ranged from 1.0 to 3.01, reflecting ease of synthesis with minimal structural complexity

Table XII. Drug-likeness parameters and synthetic accessibility of the compounds.

Compounds	Drug-likeness						Synthetic Accessibility
	MW (g/mol)	TPSA (Å ²)	ESOL Log S	Fraction Csp3	Rotatable Bonds	Bioavailability Score	
I	126.11	60.69	-1.92	0	0	0.55	1
II	240.42	12.53	-5.1	1	13	0.55	2.86
III	258.44	29.46	-4.35	1	15	0.55	3.01
IV	140.14	49.69	-1.38	0.14	1	0.55	1.33
V	126.11	50.44	-0.54	0.17	2	0.55	2.25
VI	126.11	65.98	-1.27	0.2	1	0.85	1.53
VII	240.42	17.07	-4.85	0.94	14	0.55	2.26
VIII	126.11	50.44	-1.17	0.17	0	0.55	2.39
IX	270.45	26.3	-5.13	0.94	14	0.55	2.53
X	270.45	26.3	-5.18	0.94	15	0.55	2.53

Table XIII shows the absorption parameters of the compounds displaying the solubility class and consensus values for lipophilicity and water solubility. The lowest lipophilicity value was exhibited by Compound V (0.19), while the highest by Compound X (5.54). The consensus water solubility value ranged from -0.63 to -6.32, with Compounds V and X having the least and highest, respectively. Most compounds fall within the very soluble class, with three being moderately soluble and only two being poor soluble.

The absorption potential of the compounds was assessed by the lipophilicity and water solubility defining the solubility class. The lipophilicity prediction of the SwissADME server utilizes the partition coefficient between n-octanol and water

(log Po/w) via five models: XLOGP3, WLOGP, MLOGP, SILICOS-IT, and LOGP³⁶. For our study, the consensus (log Po/w) value of the five models was used, reflecting the average of the five models. The consensus value of ESOL, Ali, and SILICOS-IT models was used for the water solubility prediction. The solubility is defined based on the log S scaled as <-10 - poorly soluble, <-6 - moderately soluble, <-4 - soluble, <-2 - very soluble, and <0 highly soluble³⁶. In our study, five (half) of the compounds were predicted to be very soluble, and out of the other half, three were moderately soluble, while only two were poorly soluble. Water solubility is an essential factor to consider in the absorption and delivery of both oral and parenteral administration drugs. Additionally, solubility contributes to ease in handling and formulation during drug development. Most of the compounds from our study might be good candidates for further development considering their solubility, while the others might require further structural modification considering their bioavailability score and structural accessibility.

Table XIII. Absorption parameters of the compounds.

Compounds	Lipophilicity (Consensus Log P _{ow})	Water Solubility (Consensus Log S)	Solubility Class
I	0.7	-1.56	Very soluble
II	5.48	-6.05	Moderately soluble
III	4.79	-5.48	Moderately soluble
IV	0.87	-1.27	Very soluble
V	0.19	-0.63	Very soluble
VI	0.31	-1.22	Very soluble
VII	5.43	-2.56	Moderately soluble
VIII	0.55	-1.19	Very soluble
IX	5.48	-6.11	Poorly soluble
X	5.54	-6.32	Poorly soluble

The distribution parameters of the compounds are presented in **Table XIV**, showing gastrointestinal (GI) absorption, blood-brain barrier (BBB) permeation, and skin permeation. All the compounds were predicted to have high GI absorption. Only Compounds II, V, VI, and VII were not BBB permeants among the compounds. The permeation values ranged from 2.55 to 7.48 cm/s, with Compound II exhibiting the most negligible value while Compound V was the highest.

Distribution of drugs across different barriers such as hepatocytes, gastrointestinal epithelial cells, blood capillary wall, glomerulus, and blood-brain barrier are the most restrictive of all. For skin permeability, the more negative the log Kp value, the less permeant the compound is predicted to be⁵⁸, while the boiled egg model was employed for the passive human gastrointestinal absorption (HIA) and blood-brain barrier (BBB) permeation⁵⁹. All the compounds from our study were predicted to possess high GI absorption, whereas only four were non-BBB permeant. Furthermore, the skin permeable was the less soluble compound revealed in **Table XIV**. The metabolic potential of the compounds was predicted by the probability of binding the compounds to the permeability glycoprotein (P-gp) or inhibition of the cytochrome P450 (CYP) isoenzymes³⁶.

Table XIV. Distribution parameters of the compounds.

Compounds	GI Absorption	BBB Permeant	Skin Permeation (Log Kp; cm/s)
I	High	Yes	-6.17
II	High	No	-2.55
III	High	Yes	-3.48
IV	High	Yes	-6.82
V	High	No	-7.48
VI	High	No	-6.73
VII	High	No	-2.76
VIII	High	Yes	-7.01
IX	High	Yes	-2.84
X	High	Yes	-2.71

The metabolic parameters of the compounds are presented in **Table XV**, showing their predicted probability of being the substrate of P-glycoprotein substrate (P-gp) and inhibitors of cytochrome P enzymes. None of the compounds were predicted to be the substrate of P-gp. Compounds II, III, VII, IX, and X were predicted to be substrates of CYP1A2 while are substrates of CYP2C19 and CYP2C9. Only Compound III was predicted to be the substrate of CYP2D6, while Compounds I, IV, and VIII for CYP3A4.

The metabolism of drugs influences their bioavailability via drug-drug or drug-protein interactions. The P-gp plays a critical role in the efflux of drugs across membranes, synergistically eliminating drugs from the body along with CYP enzymes via biotransformation⁶⁰. Considering the role of the CYP enzymes, their inhibition by drugs might contribute to the adverse effects and reactions of drugs due to their accumulation and decreased solubility. Although none of the compounds were predicted to be a substrate of P-gp, five of the compounds were inhibitors of CYP1A2, two were inhibitors of CYP3A4, one for CYP2D6, while none were inhibitors of CYP2C19 and CYP2C9, thus weakening their drug candidacy.

Table XV. Metabolism parameters of the compounds.

Compounds	P-gp Substrate	CYP1A2 inhibitor	CYP2C19 inhibitor	CYP2C9 inhibitor	CYP2D6 inhibitor	CYP3A4 inhibitor
I	No	No	No	No	No	Yes
II	No	Yes	No	No	No	No
III	No	Yes	No	No	Yes	No
IV	No	No	No	No	No	Yes
V	No	No	No	No	No	No
VI	No	No	No	No	No	No
VII	No	Yes	No	No	No	No
VIII	No	No	No	No	No	Yes
IX	No	Yes	No	No	No	No
X	No	Yes	No	No	No	No

The predicted LD₅₀, toxicity class, and endpoints of the compounds are presented in **Table XVI**. Compounds II, VII, IX, and X exhibited the highest (5000 mg/kg) LD₅₀, all within toxicity class 5, while the least was Compound VIII (220 mg/kg) within class 3. Only Compound VI was predicted to be hepatotoxic among the compounds, while Compounds I, II, III, V, and VIII were carcinogenic. Compounds I, V, and VIII were predicted to be mutagenic. However, none of the compounds show immunotoxicity and cytotoxicity.

Toxicity is an essential yet expensive stage in drug discovery. However, an *in silico* study reduces the cost and time required for this stage⁶¹. Although *in silico* toxicity study predicts the possible toxicity of compounds, further studies, including *in vivo* and *in vitro*, are required to ascertain their toxicity further. The toxicity of the compounds evaluated by the ProTox online server predicted most of the compounds to have LD₅₀ above 1000 mg/kg, with only three having ≤500 mg/kg. The LD₅₀ is the dose at which the exposed subject dies, while the toxicity class classifies from 1 to 6, with 1 being highly toxic and 6 being non-toxic. For our study, the toxicity ranged from moderately toxic to non-toxic (3 to 6), supporting their drug candidacy⁶². Furthermore, the compounds' hepatotoxicity, carcinogenicity, immunotoxicity, mutagenicity, and cytotoxicity were evaluated to predict their toxicity further. Among the compounds, only Compound VI was predicted to be hepatotoxic. Four compounds were carcinogenic; three showed mutagenicity, while none were immunotoxic or cytotoxic.

Table XVI. LD₅₀, toxicity class, and toxicity endpoints of the compounds.

Compounds	LD ₅₀ (mg/kg)	Toxicity Class	HPT	CGN	IMT	MGN	CIT
I	300	3	-	+	-	+	-
II	5000	5	-	+	-	-	-
III	2280	5	-	+	-	-	-
IV	550	4	-	-	-	-	-
V	2500	5	-	+	-	+	-
VI	1000	4	+	-	-	-	-
VII	5000	5	-	-	-	-	-
VIII	220	3	-	+	-	+	-
IX	5000	5	-	-	-	-	-
X	5000	5	-	-	-	-	-

Note: + = Active - = Inactive, HPT = Hepatotoxicity, CGN = Carcinogenicity, IMT = Immunotoxicity, MGN = Mutagenicity CIT = Cytotoxicity.

CONCLUSION

Conclusively, the compounds from *A. leiocarpus* showed good binding interactions, and the protein targets of antidiabetic therapy are potentially good candidates for antidiabetic drug development, considering the results of the molecular docking and molecular dynamics simulations. Furthermore, the antidiabetic drug potential of the compounds evaluated by the ADME study further supports the drug candidacy of the compounds, considering the results of the drug-likeness, synthetic

ability, solubility, absorption, and metabolic parameters. Additionally, the compound's toxicity results showing moderate to non-toxicity, further supports the potential of the compounds as antidiabetic drug candidates.

ACKNOWLEDGMENT

None.

AUTHORS' CONTRIBUTION

All authors have an equal contribution to carrying out this study.

DATA AVAILABILITY

None.

CONFLICT OF INTEREST

The authors declare no conflict of interest.

REFERENCES

1. American Diabetes Association Professional Practice Committee. Diabetes Care. 2022;45(Suppl 1):S17-38. doi:10.2337/dc22-s002
2. Banday MZ, Sameer AS, Nissar S. Pathophysiology of diabetes: An overview. Avicenna J Med. 2020;10(4):174-88. doi:10.4103/ajm.ajm_53_20
3. Sun H, Saeedi P, Karuranga S, Pinkepank M, Ogurtsova K, Duncan BB, et al. IDF Diabetes Atlas: Global, regional and country-level diabetes prevalence estimates for 2021 and projections for 2045. Diabetes Res Clin Pract. 2022;183:109119. doi:10.1016/j.diabres.2021.109119
4. Maiti S, Akhtar S, Upadhyay AK, Mohanty SK. Socioeconomic inequality in awareness, treatment and control of diabetes among adults in India: Evidence from National Family Health Survey of India (NFHS), 2019-2021. Sci Rep. 2023;13(1):2971. doi:10.1038/s41598-023-29978-y
5. Schellenberg ES, Dryden DM, Vandermeer B, Ha C, Korownyk C. Lifestyle interventions for patients with and at risk for type 2 diabetes: a systematic review and meta-analysis. Ann Intern Med. 2013;159(8):543-51. doi:10.7326/0003-4819-159-8-201310150-00007
6. American Diabetes Association. 9. Pharmacologic Approaches to Glycemic Treatment: Standards of Medical Care in Diabetes – 2020. Diabetes Care. 2020;43(Suppl 1):S98-110. doi:10.2337/dc20-s009
7. American Diabetes Association. 3. Prevention or delay of type 2 diabetes: Standards of Medical Care in Diabetes – 2021. Diabetes Care. 2021;44(Suppl 1):S34-9. doi:10.2337/dc21-s003
8. Dahiru MM, Samuel NM. A review of the Mechanisms of Action and Side Effects of Anti-diabetic Agents. Trends Pharm Sci. 2022;8(3):195-210. doi:10.30476/tips.2022.95931.1153
9. Wu Y, Ding Y, Tanaka Y, Zhang W. Risk factors contributing to type 2 diabetes and recent advances in the treatment and prevention. Int J Med Sci. 2014;11(11):1185-200. doi:10.7150/ijms.10001

10. Mohammed A, Tajuddeen N. Antidiabetic compounds from medicinal plants traditionally used for the treatment of diabetes in Africa: A review update (2015–2020). *South Afr J Bot.* 2022;146:585-602. doi:10.1016/j.sajb.2021.11.018
11. Teoh SL, Das S. Phytochemicals and their effective role in the treatment of diabetes mellitus: a short review. *Phytochem Rev.* 2018;17(5):1111-28. doi:10.1007/s11101-018-9575-z
12. Mohammed S, Yaqub A, Sanda K, Nicholas A, Arastus W, Muhammad M, et al. Review on diabetes, synthetic drugs and glycemic effects of medicinal plants. *J Med Plants Res.* 2013;7(36):2628-37. doi:10.5897/JMPR2013.5169
13. Adhikari B. Roles of alkaloids from medicinal plants in the management of diabetes mellitus. *J Chem.* 2021;2021:2691525. doi:10.1155/2021/2691525
14. Negbenebor HE, Shehu K, Mukhtar M, Oiza A, Nura S, Fagwalaw L. Ethnobotanical survey of medicinal plants used by Hausa people in the management of diabetes mellitus in Kano metropolis, northern Nigeria. *Eur J Med Plants.* 2017;18(2):1-10. doi:10.9734/EJMP/2017/28562
15. Manukumar HM, Kumar JS, Chandrasekhar B, Raghava S, Umesha S. Evidences for diabetes and insulin mimetic activity of medicinal plants: present status and future prospects. *Crit Rev Food Sci Nutr.* 2017;57(12):2712-29. doi:10.1080/10408398.2016.1143446
16. Arbab A. Review on Anogeissus Leiocarpus a Potent African Traditional Drug. *Int J Res Pharm Chem.* 2014;4(3):496-500.
17. Salih EYA, Julkunen-Tiitto R, Luukkanen O, Sipi M, Fahmi MKM, Fyhrquist PJ. Potential anti-tuberculosis activity of the extracts and their active components of Anogeissus leiocarpa (Dc.) guill. and perr. with special emphasis on polyphenols. *Antibiotics.* 2020;9(7):364. doi:10.3390/antibiotics9070364
18. Mukhtar Y, Abdu K, Maigari AK. Efficacy of Anogeissus leiocarpus (DC.) as potential therapeutic agent against Trypanosomiasis diseases: A review. *Int J Health Pharm Res.* 2017;3(3):1-9.
19. Okpekon T, Yolou S, Gleye C, Roblot F, Loiseau P, Bories C, et al. Antiparasitic activities of medicinal plants used in Ivory Coast. *J Ethnopharmacol.* 2004;90(1):91-7. doi:10.1016/j.jep.2003.09.029
20. Barku VYA, Opoku-Boahen Y, Owusu-Ansah E, Dayie NTKD, Mensah FE. In-vitro assessment of antioxidant and antimicrobial activities of methanol extracts of six wound healing medicinal plants. *J. Nat Sci Res.* 2013;3(1):74-80.
21. Tauheed AM, Mamman M, Ahmed A, Suleiman MM, Balogun EO. In vitro and in vivo antitrypanosomal efficacy of combination therapy of Anogeissus leiocarpus, Khaya senegalensis and potash. *J Ethnopharmacol.* 2020;258:112805. doi:10.1016/j.jep.2020.112805
22. Tagne MAF, Rékabi Y, Noubissi PA, Fankem GO, Akaou H, Wambe H, et al. Evaluation of antidiarrheal activity of aqueous leaf extract of Anogeissus leiocarpus on castor oil-induced diarrhea in rats. *Am J Biomed Sci Res.* 2019;3(1):27-34. doi:10.34297/AJBSR.2019.03.000629
23. Dahiru MM, Abaka AM, Artimas SP. Phytochemical Analysis and Antibacterial Activity of Methanol and Ethyl Acetate Extracts of Detarium microcarpum Guill. & Perr. *Bio Med Nat Prod Chem.* 2023;12(1):281-8. doi:10.14421/biomedich.2023.121.281-288
24. Hassan LEA, Al-Suade FS, Fadul SM, Majid AMSA. Evaluation of antioxidant, antiangiogenic and antitumor properties of Anogeissus leiocarpus against colon cancer. *J Angiotherapy.* 2018;1(2):56-66. doi:10.25163/angiotherapy.1200021526100818
25. Motto AE, Lawson-Evi P, Bakoma B, Eklü-Gadegbeku K, Aklíkokou K. Antihyperlipidemic and antioxidant properties of hydro-alcoholic extracts from Anogeissus leiocarpus (Combretaceae). *Heliyon.* 2021;7(4):e06648. doi:10.1016/j.heliyon.2021.e06648

26. Motto AE, Lawson-Evi P, Eklu-Gadegbeku K. Antidiabetic and antioxidant potential of total extract and supernatant fraction of the roots of *Anogeissus leiocarpus* in HFD-fed and Streptozocin-induced diabetic rats. *Biomed Pharmacother.* 2022;154:113578. doi:10.1016/j.biopha.2022.113578
27. Num-Adom SM, Adamu S, Aluwong T, Ogbuagu NE, Umar IA, Esievo KAN. Ethanolic extract of *Anogeissus leiocarpus* ameliorates hyperglycaemia, hepato-renal damage, deranged electrolytes and acid-base balance in alloxan-induced diabetes in dogs. *Sci Afr.* 2022;16:e01183. doi:10.1016/j.sciaf.2022.e01183
28. Dahiru MM, Badgal EB, Neksumi M. Phytochemical Profiling And Heavy Metals Composition Of Aqueous and Ethanol Extracts of *Anogeissus Leiocarpus*. *J Fac Pharm Ankara Uni.* 2023;47(2):311-23. doi:10.33483/jfpau.1205941
29. O'Boyle NM, Banck M, James CA, Morley C, Vandermeersch T, Hutchison GR. Open Babel: An open chemical toolbox. *J Cheminform.* 2011;3:33. doi:10.1186/1758-2946-3-33
30. Sanner MF. Python: a programming language for software integration and development. *J Mol Graph Model.* 1999;17(1):57-61.
31. Pratama MRF, Sutomo S. Chemical Structure Optimization of Lupeol As ER- α and HER2 Inhibitor. *Asian J Pharm Clin Res.* 2018;11(6):298-303. doi:10.22159/ajpcr.2018.v11i6.24226
32. Adasme MF, Linnemann KL, Bolz SN, Kaiser F, Salentin S, Haupt VJ, et al. PLIP 2021: Expanding the scope of the protein-ligand interaction profiler to DNA and RNA. *Nucleic Acids Res.* 2021;49(W1):W530-4. doi:10.1093/nar/gkab294
33. Ortiz CLD, Completo GC, Nacario RC, Nellas RB. Potential Inhibitors of Galactofuranosyltransferase 2 (GlfT2): Molecular Docking, 3D-QSAR, and In Silico ADMETox Studies. *Sci Rep.* 2019;9(1):17096. doi:10.1038/s41598-019-52764-8
34. Kurcinski M, Oleniecki T, Ciemny MP, Kuriata A, Kolinski A, Kmiecik S. CABS-flex standalone: a simulation environment for fast modeling of protein flexibility. *Bioinformatics.* 2019;35(4):694-5. doi:10.1093/bioinformatics/bty685
35. López-Blanco JR, Aliaga JJ, Quintana-Ortí ES, Chacón P. iMODS: internal coordinates normal mode analysis server. *Nucleic Acids Res.* 2014;42(W1):W271-6. doi:10.1093/nar/gku339
36. Daina A, Michielin O, Zoete V. SwissADME: a free web tool to evaluate pharmacokinetics, drug-likeness and medicinal chemistry friendliness of small molecules. *Sci Rep.* 2017;7(1):42717. doi:10.1038/srep42717
37. Banerjee P, Eckert AO, Schrey AK, Preissner R. ProTox-II: a webserver for the prediction of toxicity of chemicals. *Nucleic Acids Res.* 2018;46(W1):W257-63. doi:10.1093/nar/gky318
38. Tamrakar AK, Maurya CK, Rai AK. PTP1B inhibitors for type 2 diabetes treatment: a patent review (2011–2014). *Expert Opin Ther Pat.* 2014;24(10):1101-15. doi:10.1517/13543776.2014.947268
39. Hussain H, Green IR, Abbas G, Adekenov SM, Hussain W, Ali I. Protein tyrosine phosphatase 1B (PTP1B) inhibitors as potential anti-diabetes agents: patent review (2015-2018). *Expert Opin Ther Pat.* 2019;29(9):689-702. doi:10.1080/13543776.2019.1655542
40. Sobhia ME, Paul S, Shinde R, Potluri M, Gundam V, Kaur A, et al. Protein tyrosine phosphatase inhibitors: a patent review (2002–2011). *Expert Opin Ther Pat.* 2012;22(2):125-53. doi:10.1517/13543776.2012.661414
41. Wan ZK, Lee J, Hotchandani R, Moretto A, Binnun E, Wilson DP, et al. Structure-Based Optimization of Protein Tyrosine Phosphatase-1 B Inhibitors: Capturing Interactions with Arginine 24. *ChemMedChem.* 2008;3(10):1525-9. doi:10.1002/cmdc.200800188

42. Ghosh P, Bhakta S, Bhattacharya M, Sharma AR, Sharma G, Lee SS, et al. A novel multi-epitopic peptide vaccine candidate against *Helicobacter pylori*: in-silico identification, design, cloning and validation through molecular dynamics. *Int J Pept Res Ther*. 2021;27(2):1149-66. doi:10.1007/s10989-020-10157-w
43. Anagnostis P, Athyros VG, Tziomalos K, Karagiannis A, Mikhailidis DP. The pathogenetic role of cortisol in the metabolic syndrome: a hypothesis. *J Clin Endocrinol Metab*. 2009;94(8):2692-701. doi:10.1210/jc.2009-0370
44. Julian LD, Wang Z, Bostick T, Caille S, Choi R, DeGraffenreid M, et al. Discovery of Novel, Potent Benzamide Inhibitors of 11 β -Hydroxysteroid Dehydrogenase Type 1 (11 β -HSD1) Exhibiting Oral Activity in an Enzyme Inhibition ex Vivo Model. *J Med Chem*. 2008;51(13):3953-60. doi:10.1021/jm800310g
45. Ferenczy GG, Kellermayer M. Contribution of hydrophobic interactions to protein mechanical stability. *Comput Struct Biotechnol J*. 2022;20:1946-56. doi:10.1016/j.csbj.2022.04.025
46. Kume S, Uzu T, Isshiki K, Koya D. Peroxisome Proliferator-Activated Receptors in Diabetic Nephropathy. *PPAR Res*. 2008;2008:879523. doi:10.1155/2008/879523
47. Chiarelli F, Marzio DD. Peroxisome proliferator-activated receptor- γ agonists and diabetes: current evidence and future perspectives. *Vasc Health Risk Manag*. 2008;4(2):297-304. doi:10.2147/vh.rm.s993
48. Liberato MV, Nascimento AS, Ayers SD, Lin JZ, Cvorov A, Silveira RL, et al. Medium Chain Fatty Acids Are Selective Peroxisome Proliferator Activated Receptor (PPAR) γ Activators and Pan-PPAR Partial Agonists. *PLoS One*. 2012;7(5):e36297. doi:10.1371/journal.pone.0036297
49. Agarwal P, Gupta R. Alpha-amylase inhibition can treat diabetes mellitus. *Res Rev J Med Health Sci*. 2016;5(4):1-8.
50. Deacon CF. Physiology and Pharmacology of DPP-4 in Glucose Homeostasis and the Treatment of Type 2 Diabetes. *Front Endocrinol*. 2019;10:80. doi:10.3389/fendo.2019.00080
51. Holst JJ. The physiology of glucagon-like peptide 1. *Physiol Rev*. 2007;87(4):1409-39. doi:10.1152/physrev.00034.2006
52. Kim NH, Kim NH. Renoprotective Mechanism of Sodium-Glucose Cotransporter 2 Inhibitors: Focusing on Renal Hemodynamics. *Diabetes Metab J*. 2022;46(4):543-51. doi:10.4093/dmj.2022.0209
53. Hsia DS, Grove O, Cefalu WT. An update on sodium-glucose co-transporter-2 inhibitors for the treatment of diabetes mellitus. *Curr Opin Endocrinol Diabetes Obes*. 2017;24(1):73-9. doi:10.1097/med.0000000000000311
54. Alssema M, Ruijgrok C, Blaak EE, Egli L, Dussort P, Vinoy S, et al. Effects of alpha-glucosidase-inhibiting drugs on acute postprandial glucose and insulin responses: a systematic review and meta-analysis. *Nutr Diabetes*. 2021;11(1):11. doi:10.1038/s41387-021-00152-5
55. van Breemen RB, Li Y. Caco-2 cell permeability assays to measure drug absorption. *Expert Opin Drug Metab Toxicol*. 2005;1(2):175-85. doi:10.1517/17425255.1.2.175
56. Alam S, Khan F. Virtual screening, Docking, ADMET and System Pharmacology studies on Garcinia caged Xanthone derivatives for Anticancer activity. *Sci Rep*. 2018;8:5524. doi:10.1038/s41598-018-23768-7
57. Ertl P, Schuffenhauer A. Estimation of synthetic accessibility score of drug-like molecules based on molecular complexity and fragment contributions. *J Cheminform*. 2009;1(1):8. doi:10.1186/1758-2946-1-8
58. Potts RO, Guy RH. Predicting skin permeability. *Pharm Res*. 1992;9(5):663-9. doi:10.1023/a:1015810312465
59. Daina A, Zoete V. A boiled-egg to predict gastrointestinal absorption and brain penetration of small molecules. *ChemMedChem*. 2016;11(11):1117-21. doi:10.1002/cmdc.201600182

60. Testa B, Kraemer SD. The biochemistry of drug metabolism—an introduction: part 3. Reactions of hydrolysis and their enzymes. *Chem Biodivers.* 2007;4(9):2031-122. doi:[10.1002/cbdv.200790169](https://doi.org/10.1002/cbdv.200790169)
61. Saeidnia S, Manayi A, Abdollahi M. The pros and cons of the in-silico pharmaco-toxicology in drug discovery and development. *Int J Pharmacol.* 2013;9(3):176-81. doi:[10.3923/ijp.2013.176.181](https://doi.org/10.3923/ijp.2013.176.181)
62. Drwal MN, Banerjee P, Dunkel M, Wettig MR, Preissner R. ProTox: a web server for the in silico prediction of rodent oral toxicity. *Nucleic Acids Res.* 2014;42(W1):W53-8. doi:[10.1093/nar/gku401](https://doi.org/10.1093/nar/gku401)